EUDP Project: Low Noise Airfoil - Final Report

Bertagnolio, Franck

Publication date:
2012

Document Version
Publisher's PDF, also known as Version of record

EUDP Project `Low Noise Airfoil' – Final Report

DTU Wind Energy E-Report

BERTAGNOLIO Franck (Editor)
DTU Wind Energy-E-0004
June 2012

DTU Wind Energy
Department of Wind Energy

Author: BERTAGNOLIO Franck (Editor)
Title: EUDP Project `Low Noise Airfoil' - Final Report
Department: DTU Wind Energy

Report number:
DTU Wind Energy-E- 0004
Publication date:
June 2012

Abstract (max. 2000 char.):
This document summarizes the scientific results achieved during the EUDP-funded project `Low-Noise Airfoil'. The goals of this project are, on one side to develop a measurement technique that permits the evaluation of trailing edge noise in a classical aerodynamic wind tunnel, and on the other side to develop and implement a design procedure to manufacture airfoil profiles with low noise emission. The project involved two experimental campaigns: one in the LM Wind Power wind tunnel, a classical aerodynamic wind tunnel, in Lunderskov (DK), the second one in the Virginia Tech Stability Wind Tunnel at the Aerospace and Ocean Engineering Department of Virginia Tech (Blacksburg, VA, USA), also a classical aerodynamic wind tunnel but equipped with an anechoic chamber that allow to perform acoustic measurements. On the theoretical side, the above experiments yield a series of model validations and improvements. In particular, the so-called TNO trailing edge noise model could be significantly improved by introducing turbulence anisotropy in its formulation, as well as the influence of the boundary layer mean pressure gradient. This two characteristics are inherent to airfoil flows but were neglected in the original approach. In addition, the experimental results are confronted to detailed Large Eddy Simulations of the airfoil flow giving more insight into the flow turbulence characteristics. The methodology which consists in measuring surface pressure spectra directly on the airfoil surface using flush-mounted microphones in order to evaluate far-field noise emission using additional theoretical results has been validated. This technique presents the advantage that it can easily be used in a classical aerodynamic wind tunnel and does not require the use of an anechoic facility. It was developed as a substitute to the original plan that consisted in measuring acoustic waves using hot-wire velocimetry. This last technique proved ineffective in the LM Wind Tunnel as the high ambient noise levels largely overwhelmed the signal of interest. Finally, a new airfoil design was proposed based on a design concept including noise reduction. The new airfoil proved to perform better aerodynamically but noise reduction were not as important as expected, mainly due to the inaccuracy of the simplified flow model used in the design algorithm.

ISBN 978-87-92896-03-2
EAN 9788792896032

Contract no.:
EUDP Jr. Nr. 64009-0272

Project no.:
PSP-Elt. 1110076

Sponsorship:
EUDP-2009-II Project: `Low Noise Airfoil Design and Validation'

Cover :

Pages: 64
Figures: 40
Tables: 0
References: 70

Technical University of Denmark
Risø Campus
Frederiksborgvej 399
4000 Roskilde
Denmark
Telephone +45 46775085
info@vindenergi.dtu.dk
www.vindenergi.dtu.dk

Contents

1 Introduction

The EUDP-founded project 'Low Noise Airfoil' has been officially running from January 2010 to December 2011. It is more precisely entitled: 'Development of a Measurement Technique for Low Noise Airfoil Design and Validation'. The overall aim of the project is to design low-noise wind turbine blades and make Danish wind turbines blades more competitive in the future world wind energy market. To achieve this, the project focuses on the development of a measurement technique that allows the evaluation of blade generated noise in an industrial aerodynamic wind tunnel instead of developing a specific anechoic wind tunnel. An alternative would be to rent such a specifically designed wind tunnel facility to perform acoustic measurements, but it must be beared in mind that access to these wind tunnels is expensive. The objective is two-fold: Firstly, the above experimental methodology is used to validate engineering models that are subsequently applied to design low-noise wind turbine blades. Secondly, the designed airfoil from the blade manufacturer are tested with respect to noise before large scale industrial production occurs.

The project was initially divided into 3 main tasks:

1. Analysis of preliminary results
   As part of previous state-funded projects between Risø-DTU, LM Glasfiber and DTU-MEK (among others), various measurements related to noise emission were performed both in wind tunnels and on a real wind turbine. In this task, the above results are analyzed and used as reference for the present project. Comparisons between existing engineering models are performed. This study is used as a benchmark to evaluate these models. As part of this task, the methodology for measuring noise in a classical aerodynamic wind tunnel should be designed in view of the above measurements.

2. Development of a noise measurement technique
   This experiment is intended to demonstrate the feasibility of the proposed methodology, i.e. measuring noise inside an aerodynamic wind tunnel. Three different airfoils are to be tested. This step is mandatory in order to ensure that the method can differentiate between these different airfoils, each characterized by a different acoustic signature.
   In addition, the experimental data related to the actual sources of noise and obtained during this campaign are used and correlated with the noise signature measurements to better understand the mechanism involved in noise generation and further refine the model theories.

3. Low-noise wind turbine airfoil and proof of concept
   It is intended to design an airfoil specifically tailored for low-noise characteristics, without compromising its aerodynamic performances. This airfoil is finally be tested in a wind tunnel to prove the potential of the proposed design and verification of concept.

The above plan was modified to some extent due to technical difficulties that arose during the first experiment of the project. In particular, the approach intended to be used to evaluate noise in Task.2 was based on a two-step method. Firstly, the noise sources should be evaluated using surface microphones flush-mounted in the airfoil near the trailing edge. In theory, this should characterize the turbulence in the boundary layer that will subsequently radiate as noise to an extent that it is nearly sufficient to evaluate the radiated noise. Secondly, the far-field noise was supposed to be measured with a second measurement device. The latter plan of action relied on two hot-wire probes that would be inserted

in the wind tunnel in the vicinity of the airfoil trailing edge, though outside the turbulent boundary layer in order to avoid its perturbating effect. However, the results proved to be seriously contaminated by powerful acoustic waves that were travelling in the wind tunnel. It should be reminded here that the above-described experiment was conducted in the LM Power wind tunnel at Lunderskov which is not designed for acoustic measurements, and therefore there is no special device or equipment to attenuate acoustic waves in the tunnel.

The change of plan then consisted in only relying on the surface microphones to evaluate noise emission using theoretical results. Nevertheless, this approach needed to be validated. It was therefore decided to use a wind tunnel (located at Virginia Tech. University, USA) where such acoustic measurements could be performed within a classical aerodynamic wind tunnel.

This report is organized as follows. The various modeling and experimental studies and their main results are provided in each of the report sections. These deals with the following topics:

- Experiment in LM Wind Tunnels including the hot-wire measurements useful to characterize the turbulent boundary layer around an airfoil and how these are correlated to the surface pressure measurements with microphones near the trailing edge; the failed noise measurements using hot-wire is presented.
- The results of the above experiment, in particular hot-wire measurements inside the boundary layer, are compared with detailed Large Eddy Simulations of the flow around the airfoil.
- Anisotropic model development, including boundary layer pressure gradient influence, and using the above results to tune the model.
- Noise evaluation technique based on surface pressure fluctuations measurement using microphones.
- Design of a new low-noise/aerodynamic efficient airfoil using a classical optimization method in which noise evaluation has been included.
- Validation in Virginia Tech wind tunnel:
    - Validation of the far-field noise evaluations based on surface pressure measurements.
    - Validation of the low-noise airfoil design.

This report is terminated by general conclusions and perspectives.

2 Wind Tunnel Measurements at LM Wind Power

Author: F. Bertagnolio

This section presents the results obtained during the experimental campaign that was conducted in the wind tunnel at LM Wind Power in Lunderskov from August 16^{th} to 26^{th}, 2010. The goal of this study is to validate the so-called TNO trailing edge noise model through measurements of the boundary layer turbulence characteristics and the far-field noise generated by the acoustic scattering of the turbulent boundary layer vorticies as they convect past the trailing edge.

This campaign was conducted with a NACA0015 airfoil section that was placed in the wind tunnel section. It is equipped with high-frequency microphones beneath its surface so that surface pressure fluctuations generated by the boundary layer turbulence can be measured.

Hot-wire anemometry was used to measure mean flow velocities and turbulent fluctuations inside the boundary layer. For this, a traverse system was developped so that the hot-wire probes could be moved with a step motor perpendicularly to the airfoil chord in order to perform measurements across the boundary layer. The probes could be moved manually back and forth relatively to the inflow velocity and along the trailing edge in order to investigate several locations in the flow field.

As a second part of the experiment, the previous traverse system was removed and two airfoil-shaped probe-holders were installed instead. These were designed to hold in place two hot-wire sensors, one on each side of the trailing edge (below and above the plane spanned by the airfoil trailing edge and the inflow velocity) in an attempt to measure the velocity fluctuations associated to the pressure waves originating from the acoustic scattering at the trailing edge, which should behave as a dipole.

The results of this experiment are reported in details in the technical report by Bertagnolio [6].

2.1 Experimental Set-up

2.1.a LM Wind Power Wind Tunnel

The LM Wind Power wind tunnel is designed for the testing of wind turbine airfoils [50]. The actual test section dimensions are 1.35 m in width, 2.70 m in height, and 7 m in length. A NACA0015 airfoil section with a 0.9 m chord was placed across the width of the tunnel. During this study, three inflow velocities were investigated: $U_\infty = 30$, 40 and 50 m/s, as well as four angles of attack: $\alpha =$ 0, 4, 8 and 12^o.

A previous study [50] showed that the inflow turbulence (without turbulence grid in the tunnel as it is the case here) was roughly of the order of $I = 0.1\%$ in all velocity directions at all wind tunnel inflow velocities. A subsequent study [5] using tri-axial hot-wire anemometry showed higher turbulence intensities of approximately 1%.

2.1.b Hot-Wire Measurements

Both single-wire and bi-axial hot-wire probes from Dantec Dynamics [34] together with the StreamLine CTA (Constant Temperature Anemometer) measurement system and the StreamWare software were used for data acquisition and post-processing. The traverse system used to explore the boundary layer (BL)

with these probes was designed and manufactured at Risø DTU by Andreas Fischer. The whole system with probes installed in the wind tunnel downstream of the airfoil trailing edge (TE) is pictured in Figure 1.

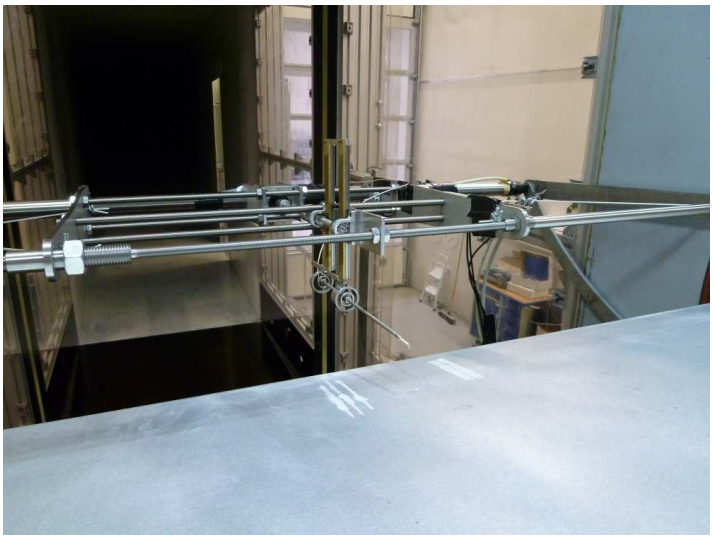

Figure 1. Traverse set-up

As for the far-field sound measurements, two slanted hot-wire probes were fixed at the tip of probe-holders, themselves mounted on the nose of airfoil-shaped holders spanning the whole tunnel width downstream the airfoil TE. The device set-up can be seen in Fig. 2.

Figure 2. Slanted hot-wire holders set-up

2.1.c Airfoil Model and Surface Microphones

The NACA0015 airfoil section with a chord $C = 0.9\,\mathrm{m}$ and a spanwise extension $L = 1.35\,\mathrm{m}$ was installed in the wind tunnel. Sennheiser KE 4-211-2 microphones were flush-mounted beneath the airfoil surface in order to measure the pressure fluctuations. These microphones have a potential sampling frequency larger than 50 kHz. However, the actual sampling rate of the data was set to the same as for the hot-wire probes, i.e. 25 kHz. Note that the low-pass filter couldn't be applied

to the microphone measurement data since these were directly acquired through the A/D board and could not be processed by the StreamLine acquisition system. Consequently, the surface pressure measurements may be polluted by some aliasing effects. However, it is believed that this effect is small in our case as the energy contained in the signals at frequencies above 25 kHz is expected to be rather small.

2.2 Measurement vs. Model Comparisons

This section concentrates on comparison between the measured data (i.e. BL velocity components and surface pressure) and numerical modeling.

In a first step, CFD calculations are performed with the two-dimensional Reynolds Averaged Navier-Stokes solver EllipSys2D [63, 44, 46] using the $k-\omega$ SST turbulence model [43]. For comparison with the clean airfoil, the e^n transition model by Drela and Giles [22] is used. Mean velocity profiles and averaged turbulent quantitities are compared with measurements. In addition, the velocity spectra measured in the wind tunnel are compared with the isotropic theoretical spectra of Von Karman (or other similar derivation) for which the turbulent kinetic energy (or turbulent stresses) and length scales are extracted from the CFD calculations or the measurement data.

In a second step, the results from the previous CFD calculations can be used as input for the TNO model that provides an estimation of the surface pressure spectra (in addition to the far field noise spectra).

2.2.a Comparison with CFD Calculations

CFD results are compared with the clean airfoil experimental results. Note that the results displayed for $\alpha = 0$ and 12^o were obtained with the inflow velocity $U_\infty = 50\,\mathrm{m/s}$, and those for $\alpha = 4$ and 8^o with $U_\infty = 40\,\mathrm{m/s}$.

The mean velocity and turbulent kinetic energy (TKE) profiles are plotted in Figs. 3 and 4, respectively. The TKE for the experimental results is obtained by adding the turbulent stresses in all directions and dividing by 2. Although the computational and experimental mean velocity profiles are quite similar, the velocity difference at one given BL position can be quite large. This may be caused by a wrong offset specification of the initial probe position when exploring the BL. As for the TKE, it can be observed that the differences between computational and experimental results increase with increasing angle of attack.

The turbulent stresses in the three space directions are displayed in Figs. 5(a-b-c). Isotropy is assumed for the CFD results, that is:

$$< u_i u_i > = \frac{2}{3} k_T \qquad \text{for} \quad i = x, y, z$$

It is clear that the flow is highly anisotropic. The u_x component is noticeably more energetic than the two others, whereas the u_z component is slightly more energetic than the u_y component.

A wind tunnel blockage effect could have explained some discrepancies. However, it appears that the differences in maximum mean velocity at the top of the BL between the measurements and the calculations (see Fig. 3) are rather small. Nevertheless, the measured maximum velocity slowly overtakes the computed one as the angle of attack increases. This could be expected since the blockage effect is intensified when the apparent surface of the airfoil relatively to the incoming flow, which is directly related to the angle of attack, increases.

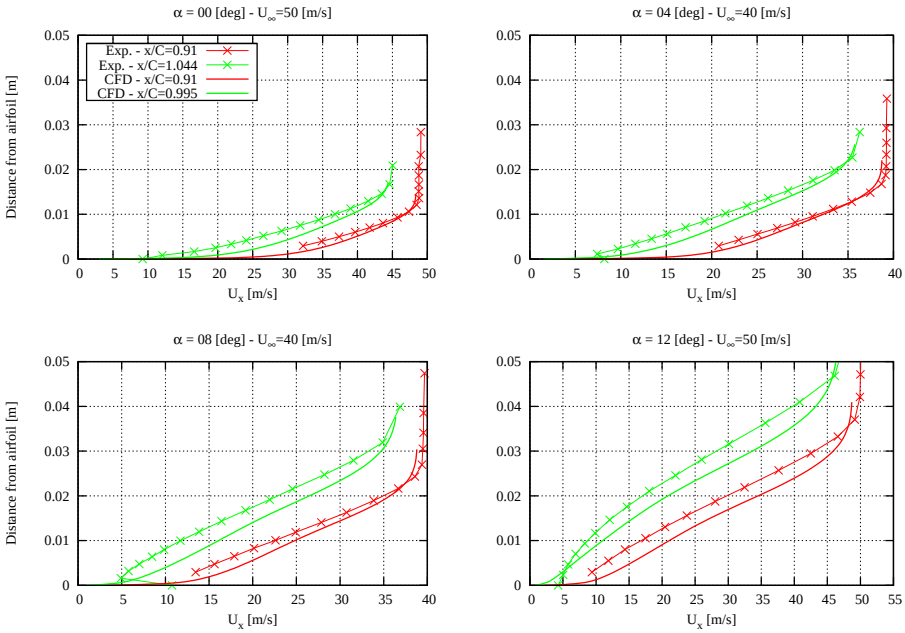

Figure 3. Velocity profile U_x

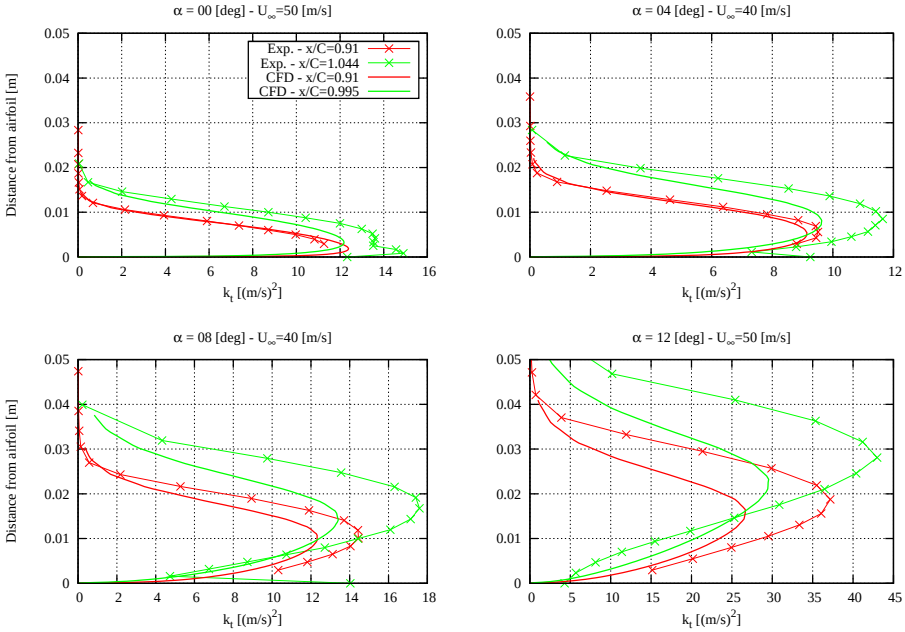

Figure 4. Turbulent kinetic energy k_T

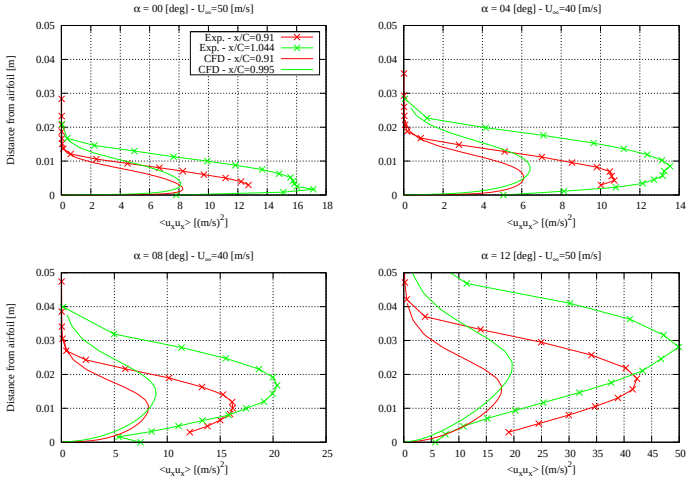

(a) Turbulent stress $< u_x u_x >$

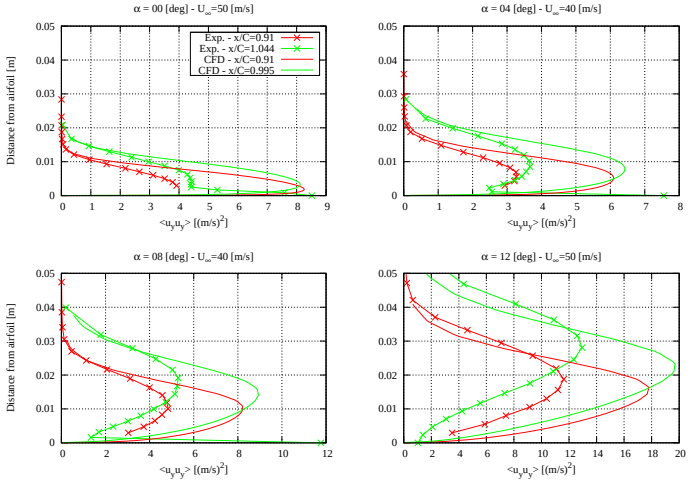

(b) Turbulent stress $< u_y u_y >$

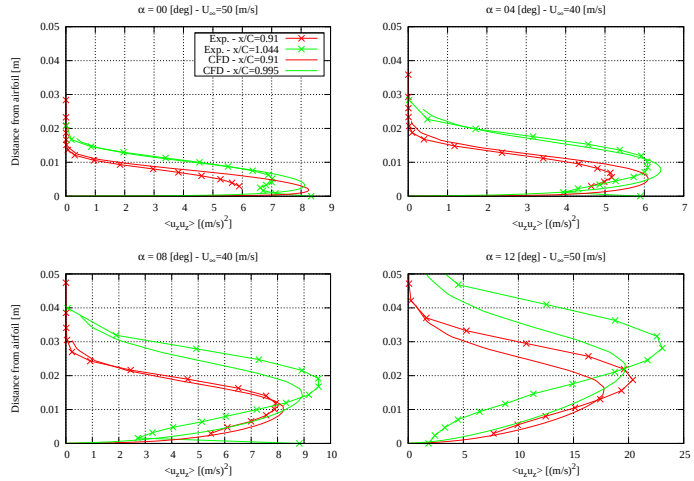

(c) Turbulent stress $< u_z u_z >$

Figure 5. Turbulent stresses (CFD: $< u_i u_i >= 2/3 \cdot k_T$)

2.2.b Measured Velocity and Isotropic One-Point Spectra

For the same cases as in the previous section, the 'pre-multiplied' (see definition below) one-point spectra of the u_x and u_y components are compared with those predicted by the theory of Von Karman for which isotropy is assumed. Note that the spectra displayed in this section are plotted as functions of the wavenumber k_1 which is parallel to the mean flow direction. By assuming frozen turbulence, the following relationship is used:

$$k_1 = 2\pi f / U_x$$

where f is the frequency and U_x is the local mean flow velocity. In addition, all spectra are 'pre-multiplied' by k_1 in order to make their peak wavenumber values, which is characteristics of the integral length scale, appear more clearly in the figures.

The definition of the Von Karman spectrum requires the variance of the considered velocity component, as well as the corresponding integral length scale. These can be extracted either from the experimental or from the CFD calculation results. As mentioned above, the peak value wavenumber of the spectra is characteristic of the integral length scale, whereas the amplitude of the spectra is characteristic of the turbulence intensity (variance) of the specific velocity component.

Fig. 6(a) shows the spectra for the u_x component, and Fig. 6(b) for the u_y component. The Von Karman spectra are evaluated using the experimental turbulent stresses and integral length scales. The agreement between the experimental and theoretical spectra is very good for the u_x component. As for the u_y component, the figures indicate in most cases a shift of the theoretical spectra toward higher wavenumbers, indicating that the evaluated integral length scale is too small or alternatively, that the Von Karman spectrum is not a good approximation for this component.

Fig. 7(a-b) show the same spectra as above for the u_x and u_y components, respectively. However, the Von Karman spectra are now evaluated using the turbulent stresses and integral length scales extracted from the CFD calculations. It must be noted here that these data were not extracted at the same distance to the wall for which the measured spectra are shown, but where the mean flow velocities coincide (The actual BL locations are indicated in the figure's legends). This is done because some small errors in the offset defining the initial distance of the probe to the wall yield large error in the turbulent quantities evaluation, since these quantities vary very rapidly close to the wall. In addition, the CFD calculations only give access to the vertical integral length scale L_2 (see Section 4.1.a) and the turbulent kinetic energy. Here, isotropy is assumed and the same values are used in both x and y-directions . The following computational values are used as input for the Von Karman one-point spectra definition:

$$L = \frac{1}{0.7468}\, L_2 \qquad \text{and} \qquad < u_i u_i > = \frac{2}{3}\, k_T$$

The agreement is now much more mitigated than before. As for the u_x component, there exists a noticeable shift of the theoretical spectra toward higher wavenumbers and the amplitudes of the theoretical spectra seem also to be largely underestimated. As for the u_y component, the agreement is slightly better, but a small shift of the theoretical spectra to the higher wavenumber still exists and this time, their amplitudes is slightly overestimated. These remarks apply to the two locations closest to the surface. Conclusions are somehow different for the location furthest away (but this is less critical, as far as the TNO model is concerned, since the influence of this location on the surface pressure is largely reduced due to its larger distance to the wall and the local turbulence intensity is relatively low anyway).

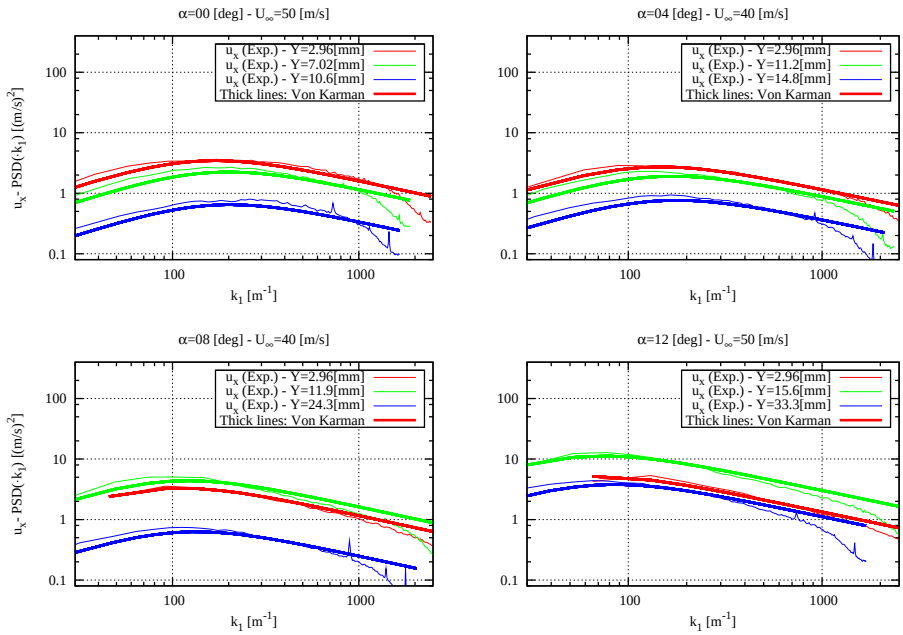

(a) u_x component

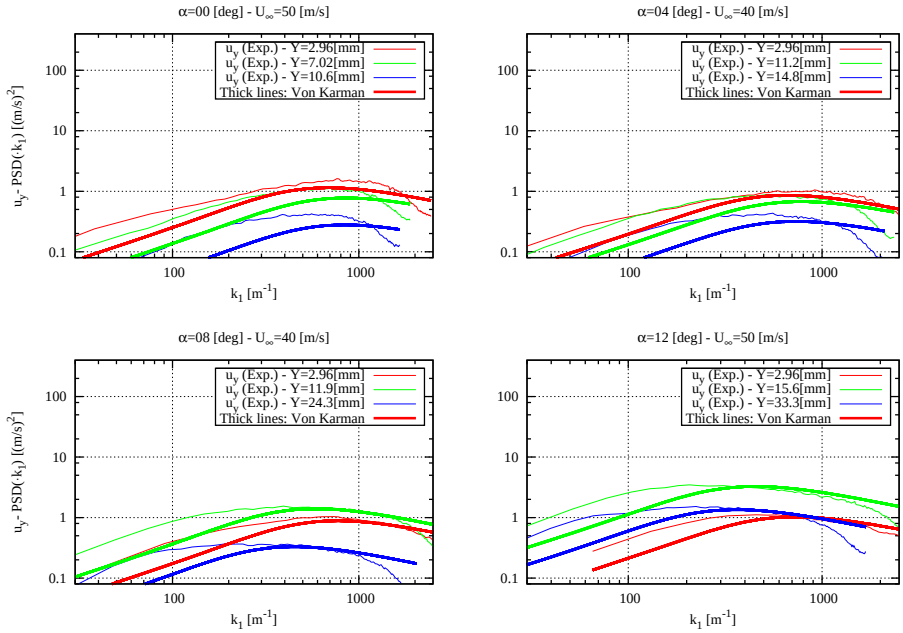

(b) u_y component

Figure 6. Pre-multiplied one-point spectra (V.K. using experimental data)

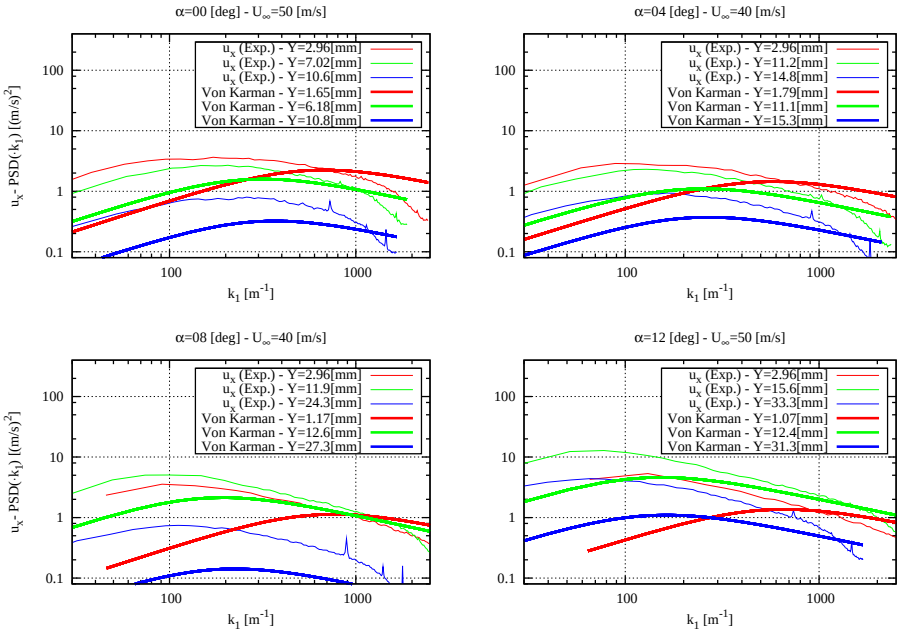

(a) u_x component

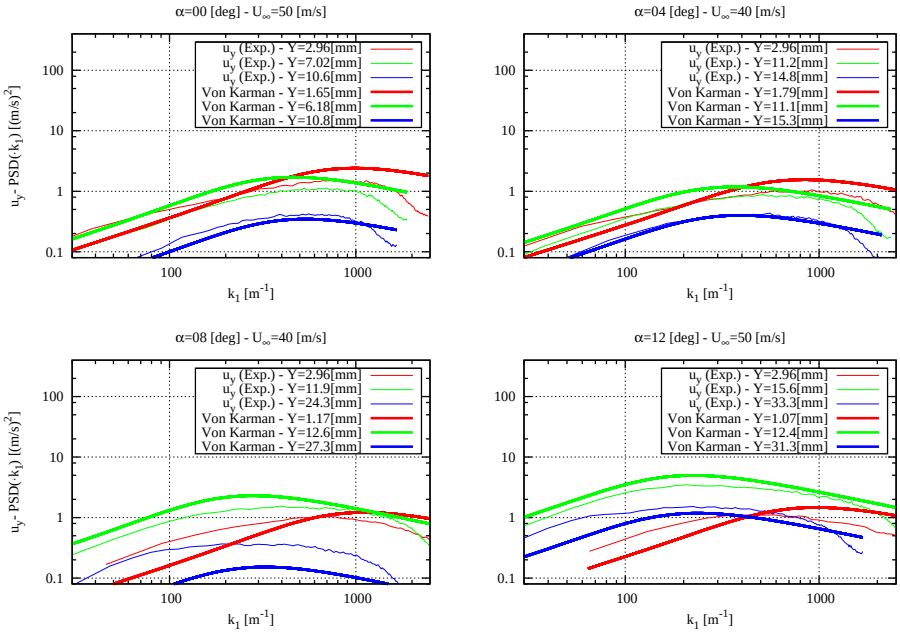

(b) u_y component

Figure 7. Pre-multiplied one-point spectra (V.K. using CFD data)

2.2.c Surface Pressure and CFD/TNO Model

As described in Section 4.1.a, the TNO model gives access to the surface pressure fluctuations spectra. These spectra could be reliably measured during the present campaign. In this section, both sets of data are compared at the chord location $X/C=0.894$. Note that all input flow data for the TNO model have been obtained with CFD calculations. In these calculations, the transition is determined with the e^n transition model by Drela and Giles [22] and the parameter N_{crit} is set to 9.

The surface pressure spectra obtained with the original CFD/TNO model are compared with the measurements at the chord location $X/C=0.894$ in Fig. 2.2.c. Each of the four subfigures corresponds to one of the considered angles of attack $\alpha = 0, 4, 8$ and 12^o. In each subfigure, results for the three wind tunnel inflow velocities are plotted. It can be observed that the surface pressure is consistently underestimated by the model, and that this underestimation is increasing as the angle of attack increases. However, the form of the measured spectra is quite well predicted by the model. Indeed, the evolution of the spectra (i.e. the spectrum slope at higher frequencies and the spectrum peak frequency) as a function of the angle of attack is very well reproduced by the model, as well as the increasing spectral intensity as a function of the inflow velocity.

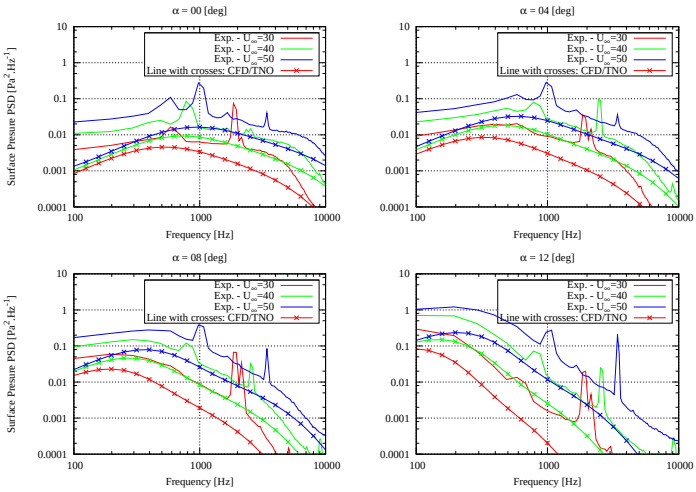

2.2.d Conclusions on BL Measurements

The various tests performed in this section to evaluate the impact of the various parameters on the CFD/TNO model prediction of the surface pressure spectra, together with the comparisons of CFD results with BL measurements provide some indications on how to improve the TNO model.

It seems clear from Section 2.2.a that the CFD calculations underestimate the TKE in the turbulent BL when the angle of attack is getting large. This underestimation is increasing as the angle of attack is increasing, which is correlated to the fact that the CFD/TNO model underestimates the surface pressure spectra as the angle of attack increases. However, attempts to increase the TKE (within sensible limits) were not successfull in reducing the discrepancies between measured and modeled surface pressure spectra at high angles of attack.

It is also clear that the isotropic assumption might be in default here.

2.3 Trailing Edge Noise Measurements

As described in Section 2.1, two slanted single hot-wire probes were placed in the wind tunnel near the trailing edge (TE) of the airfoil, one on each side of the TE relatively to the airfoil chord plane. Both probes were located outside of the BL and wake generated by the airfoil itself so that BL/wake turbulence will not affect the measured velocity fluctuations.

The goal is to measure the TE radiated noise that should behave as a dipole and therefore should be characterized as out of phase pressure/velocity fluctuations on both sides of the TE. The slanted probes are orientated so that the hot-wires stand approximately along a line perpendicular to the TE and perpendicular to the line joining the probe to the closest point on the TE. In this way, the set-up will significantly filter out waves that are not parallel to TE noise waves, though waves travelling in the direction parallel to the TE will not be filtered out. One can therefore expect that the resulting measurements will be contaminated by spurious sound waves reflecting on the side walls of the wind tunnel. In any case, it cannot be expected that this set-up will filter out all background noise present in the wind tunnel as it will become clear in the analysis of the measured data below.

In order to evaluate this measurement technique, two different configurations are investigated here. In the first one, the probes are located at approximately 9 cms below and above the plane described by the mean inflow velocity and the TE, and at a distance approximately equal to 13 cms from the TE perpendicularly to the TE direction. The angle of attack of the airfoil is equal to $\alpha = 8^o$. As for the second configuration, the probes are located at the same relative locations in the wind tunnel but the airfoil is removed from the wind tunnel.

The coherence and phase between the velocities measured by the two hot-wires are plotted in Figs. 8(a) and (b), respectively, for an angle of attack $\alpha = 8^o$ and for the empty wind tunnel at all considered inflow wind speeds $U_\infty = 30, 40$ and 50 m/s. It can be observed that there is no significant difference between the wind tunnel being empty and when the airfoil is present, except at lower frequencies ($f < 600$ Hz) where there exist strong correlated signals captured by the two hot-wires. However, the phase behaviour does not indicate that it is related to TE noise (which should be characterized by a $\pm\pi$ phase shift), but rather that it behaves more like the phase shift of sensors measuring the same traveling wave at different locations (i.e. characterized by a linear variation of the phase as a function of frequency). This latter behaviour could be the result of the two hot-wire probes being located not exactly at the same distance from the acoustic source.

A small frequency range for which the two velocities measured by the hot-wires are out of phase can be observed around $1500 < f < 2100$ Hz. However, it is also observed when the wind tunnel is empty excluding that this could be related to TE noise. In addition, sharp large coherence peaks can be observed above 2000 Hz. Their frequency locations increase with increasing inflow speed. These are most certainly caused by the wind tunnel fan noise.

The large coherence between the hot-wire signals observed at frequencies lower than approximately 600 Hz is investigated in more detail. The cross-spectra of the two signals are displayed in Fig. 9(a). It is important to note here that, for a sound wave emitted by a dipole source, the velocity is linearly related to the time derivative of the pressure field. Therefore, the velocity amplitude should scale as the pressure amplitude. In addition, the sound wave intensity (proportional to the pressure amplitude squared) of trailing edge noise should scale as U_∞^5 at higher frequencies, i.e. $f \gg c_0/C$ where C is the airfoil chord and c_0 the speed of sound (see Blake [10], Vol.II, p.732), and as U_∞^6 at lower frequencies, i.e. $f \ll c_0/C$. The cross-spectra non-dimensionalized using the two scaling laws are displayed

in Figs. 9(b) and (c), respectively. It can be observed that the two scalings give similar results, and that in both cases, the cross-spectra seem to merge into a common curve. In addition, note that the intermediate scaling frequency c_0/C is approximately equal to 380 Hz in our case. This might indicate that the highly correlated signals at low frequencies may originate from a compact acoustic source (low wavenumber acoustic waves relatively to the airfoil chord) due to the interaction of the airfoil with either inflow turbulence or turbulent boundary layer vortices convecting above the trailing edge.

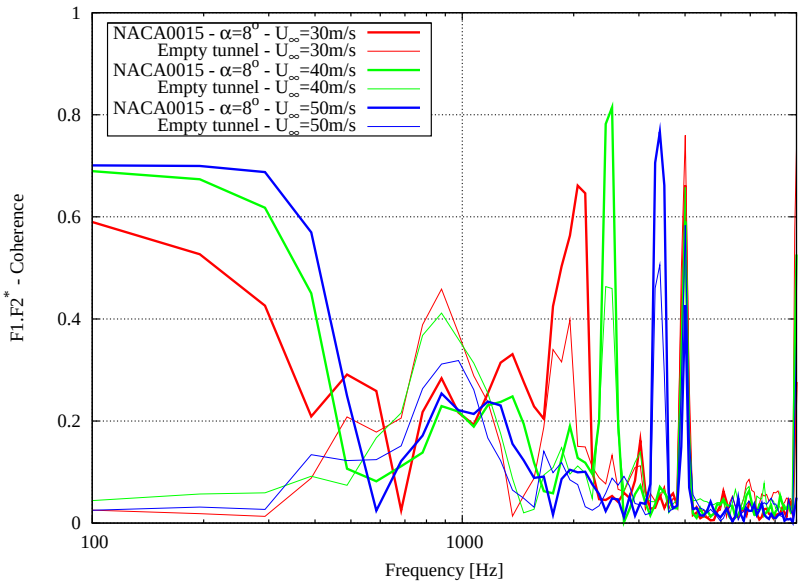

(a) Coherence

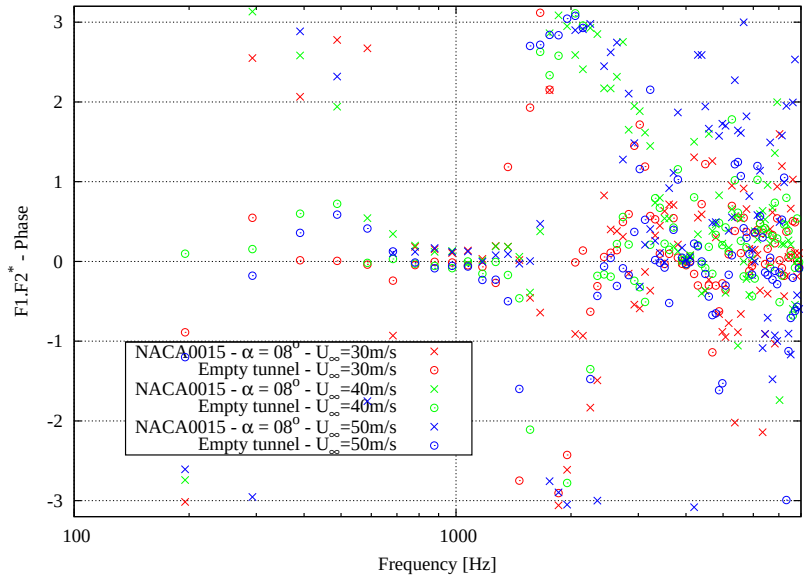

(b) Phase

Figure 8. Coherence/Phase between slanted hot-wire measured velocities - $\alpha = 8^o$ vs. empty wind tunnel

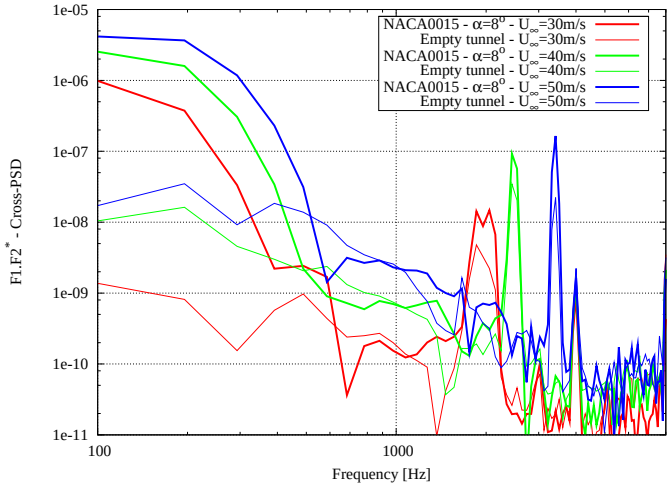

(a) Cross-PSD

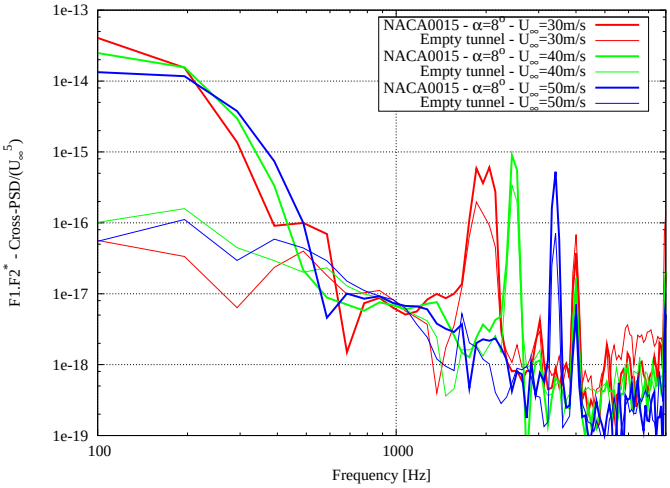

(b) Normalized Cross-PSD (Spectrum normalized by U_∞^5)

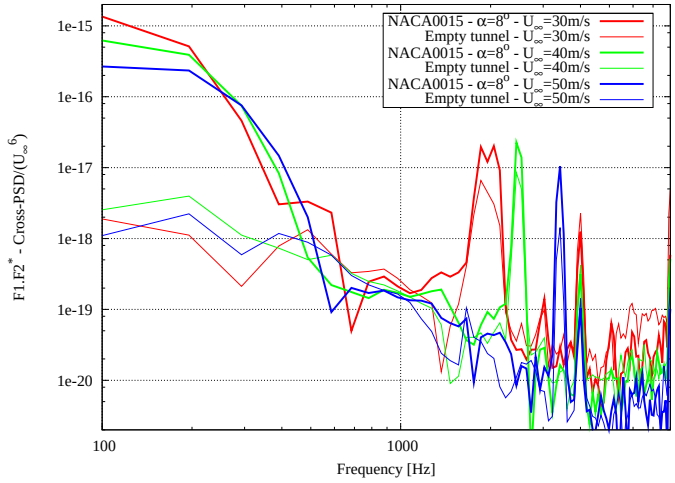

(c) Normalized Cross-PSD (Spectrum normalized by U_∞^6)

Figure 9. Cross-spectra between slanted hot-wire measured velocities - $\alpha = 8^o$ vs. empty wind tunnel

2.3.a Conclusions on Hot-Wire Noise Measurements

As a conclusion for this section, it seems that measuring trailing edge noise with the present set-up is not feasible. Some noise related to the presence of the airfoil could be measured at lower frequencies, however, it remains uncertain what its origin is. The main reason for these inconclusive results is most probably the presence of intense background noise which overwhelms the TE noise that we are trying to measure.

2.4 Conclusions

Hot-wires and surface pressure measurements of the NACA0015 airfoil that were performed in the LM wind tunnel provide a detailed description of the BL mean velocity profiles as well as BL turbulent velocity fluctuations and the associated surface pressure fluctuations. These measurements are intended to validate both the CFD calculations using the RANS code EllipSys2D and the TNO model which uses the previous calculations as an input for the evaluation of the surface pressure spectrum, and subsequently the trailing edge far-field noise. There is a relative quite good agreement between the CFD results and the measurements. Some discrepancies were observed for the turbulent kinetic energy and integral length scale distributions across the boundary layer. The TNO model predicts the qualitative features of the surface pressure as a function of inflow velocity and angle of attack quite well. However, discrepancies exists concerning the quantitative results. In particular, the modeled surface pressure spectra largely underestimate the measurements. Some corrections based on the discrepancies observed between the CFD results and the measured turbulent boundary layer quantities were implemented to improve the model. However, it proved unable to eliminate the surface pressure spectra underestimation at high angles of attack.

The second part of the experiment intended to measure trailing edge noise with hot-wire anemometry. It turns out that the background noise present in the wind tunnel (originating from the fan, boundary layer along the walls of the wind tunnel, reflecting sound waves on these walls, etc...) seems to dominate the whole frequency range where trailing edge noise should be observed. These spurious sound waves could not be filtered out. Nevertheless, sound waves related to the presence of the airfoil could be observed in the frequency range 100-600 Hz. However, their origin could not be clearly identified.

As a final conclusion, it seems that the LM wind tunnel is not adapted to measure trailing edge noise using hot-wire anemometry due to the high background noise present in the tunnel. However, the relative good agreement between the TNO modeled and the measured surface pressure using the flush-mounted airfoil microphones can indirectly give access the radiated trailing edge noise using the TNO model theory.

Acknowledgments

This experimental campaign would not have been possible without the wind tunnel facility provided by LM Wind Power and its Senior Manager Aerodynamics Peter Fuglsang, as well as the help of Olaf, Kenny and Hans.

3 Comparisons between LES and Wind Tunnel Hot-Wire Measurements

Authors: W.J. Zhu, W.Z. Shen and J.N. Sørensen

Large-eddy simulations (LES) are carried out for flows over a NACA 0015 airfoil at AoA = 8^o and a chord based Reynolds number of 1.71×10^6. To accurately simulate the complex flow on the suction side of the airfoil, a reasonably large number of grid points is required. The computational mesh is constructed in a wind tunnel similar to the LM wind tunnel where the experiment for an NACA 0015 airfoil was carried out. The goal of this study is to validate the mixed scale SGS turbulence model against detailed measurements. Simulations are performed with the in-house EllipSys3D code on high performance computers. The stability and accuracy of the LES simulations are studied on various mesh configurations. The spanwise grid spacing is found important to produce correct flow disturbances along the airfoil span, which can affect the turbulent energy distribution.

3.1 Introduction

Computational Fluid Dynamics (CFD) has entered into its mature stage. Different techniques exist to model turbulent flows: the Reynolds-averaged Navier-Stokes (RANS) method, the detached eddy simulation (DES), the large eddy simulation (LES) and the direct numerical simulation (DNS). The RANS technique is most popular for solving engineering based flow problems. One has the alternative to choose one equation models, for example the Baldwin-Barth model [3] and the Spalart-Allmaras model [65], and the two equation models, for example the k-epsilon model [35] and the k-omega model [69]. A more advanced method that combines RANS and LES is the DES method [66]. Comparing with RANS, DES is much more convincing to resolve highly separated turbulent flows. In LES, large eddies are solved explicitly and smaller eddies are treated implicitly using sub-grid-scale (SGS) models. LES does not resolve the full range of turbulence scales, but it solves a scale range much wider than RANS. The use of LES is a compromise between limited computer resource and numerical accuracy. As the grid becomes finer, the SGS Reynolds stress is smaller. The method is identical to DNS when the grid density is high enough to resolve the smallest eddy structures.

The increase of computer power and memory storage has raised the interest of using LES. LES appears to be a potential numerical tool that can handle complex turbulent flow problems. The foundation works of Smagorinsky [62], Lilly [36] and Deardorff [19] were aimed at weather forecasts. For flows with smaller scale objects, such as turbulent airfoil flows, some modified LES models were proposed. The method for modeling the SGS stress tensor is seen in Bardina et al [4]. The models of Ta Phuoc [53] and Sagaut [58] are an extension of the Smagorinsky model as well. The eddy viscosity is a function of vorticity, shear strain tensor and turbulent kinetic energy, therefore it is called mixed scale eddy viscosity model. Such approach is seen in Mary and Sagaut [40] who simulated flows over an airfoil near stall. It was found that the simulated mean and fluctuating velocity profiles compare favourably with experimental data. It was suggested that the streamwise, wall normal and spanwise mesh resolutions in terms of wall units must satisfy the grid size constrains: $x^+ < 50$, $y^+ \approx 2$, $z^+ \approx 20$, respectively. On the other hand, the values suggested by [54] are $50 < x^+ < 150$, $y^+ \approx 1$, $15 < z^+ < 40$. For

comparison, the criteria used for DNS are: $10 < x^+ < 20$, $y^+ \approx 1$, $5 < z^+ < 10$. In the above criteria, the limitation of the spanwise spacing is even more critical than in the streamwise direction. In the present paper, the mixed scale eddy viscosity model is used to investigate turbulent flows over a NACA 0015 airfoil. Numerical simulations are conducted in a wind tunnel of a similar geometry as in the experimental setup. Effects of grid spacing in the spanwise direction are investigated.

3.2 Numerical Method

3.2.a Governing Equations

In LES the filtered Navier-Stokes equations is defined as

$$\frac{\partial \bar{U}_i}{\partial t} + \frac{\partial (\bar{U}_i \bar{U}_j)}{\partial x_i} = -\frac{1}{\rho}\frac{\partial \bar{P}}{\partial x_i} + \nu \frac{\partial^2 \bar{U}_i}{\partial x_j^2} + \frac{\partial \tau_{ij}}{\partial x_j} \tag{1}$$

$$\frac{\partial \bar{U}_i}{\partial x_i} = 0 \tag{2}$$

where the first filter is identified by a bar ($^-$). The solutions obtained from equation (1) and (2) are filtered due to the finest grid level used in the computation.

The flow velocity can be written as $U_i = \bar{U}_i + U_i'$, where $\bar{U}_i$ represents the resolved scale part and U_i' is its subgrid scale part. The large scales are simulated whereas the small scales are modelled by the sub-grid-scale (SGS) model. The term that requires to model is the SGS stress

$$\tau_{ij} = \bar{U}_i\bar{U}_j - \overline{U_iU_j} = \left(\bar{U}_i\bar{U}_j - \overline{\bar{U}_i\bar{U}_j}\right) - \left(\overline{\bar{U}_iU_j' + U_i'\bar{U}_j}\right) - \overline{U_i'U_j'} \tag{3}$$

The turbulent stresses are modelled with an eddy viscosity

$$\tau_{ij} = \nu_t \left(\frac{\partial \bar{U}_i}{\partial x_j} + \frac{\partial \bar{U}_j}{\partial x_i}\right) - \frac{2}{3}k\delta_{ij} \tag{4}$$

The eddy viscosity is determined by the mixed scale turbulence model introduced by Ta Phuoc [53]

$$\nu_t = C|\overline{\vec{\omega}}|^{\alpha} k^{\frac{(1-\alpha)}{2}} \Delta^{(1-\alpha)} \tag{5}$$

where $\Delta = (\Delta_x\Delta_y\Delta_z)^{1/3}$ is an average grid size, and is a parameter that takes values in the range between 0 and 1. The turbulent kinetic energy can be estimated by using a test filter

$$k = \frac{1}{2}\sum_{j=1}^{3}\left(U_j - \bar{U}_j\right)^2 \approx \frac{1}{2}\sum_{j=1}^{3}\left(\bar{U}_j - \widetilde{\bar{U}_j}\right)^2 \tag{6}$$

where $\widetilde{\bar{U}_j}$ is the velocity resulted from the test filter. Assuming flow similarity between two grid levels, the test filter is applied on the coarser mesh which is double coarser than the finest mesh. The model equation (5) becomes a pure vorticity based model in the case when $\alpha = 1$,

$$\nu_t = C|\overline{\vec{\omega}}|\Delta^2 \tag{7}$$

and it becomes the Bardina model [4] in the case when $\alpha = 0$,

$$\nu_t = Ck^{\frac{1}{2}}\Delta \tag{8}$$

From studies on the model parameter, it was found that the model generally performs best when the parameter α is chosen to be 0.5,

$$\nu_t = C|\overline{\vec{\omega}}|^{\frac{1}{2}} k^{\frac{1}{4}} \Delta^{\frac{2}{3}} \tag{9}$$

with $C = 0.04$. Therefore, this model is used in our computations for turbulent flows.

3.2.b The Flow Solver

The EllipSys code [44, 46, 63] has been developed for solving general incompressible flows. The solver is based on a second-order finite volume method where the multi-grid strategy is used for solving the pressure correction equation. The code solves the velocity-pressure coupling equations with the SIMPLE/SIMPLEC/PISO method. The momentum equations are first solved with a known pressure to give a prediction and the continuity equation is used as a constraint on the velocity to obtain a pressure correction equation. In the predictor step, the momentum equations are solved by the second-order backward differentiation scheme in time and second-order central differences in space. The QUICK upwind scheme is used for the convective terms instead of using central differences schemes. In the corrector step, the improved Rhie-Chow interpolation [61] is applied to suppress numerical oscillations from velocity-pressure decoupling. Also, the improved SIMPLEC scheme for collocated grids [60] is used such that the solution is independent of the relaxation parameters and the time-step. The differential form of NS equations are transformed into a curvilinear coordinate system aligned with the local grid lines. In 3D case, the metric expressions of the partial differentials are

$$\begin{aligned}
\frac{\partial}{\partial x} &= \frac{1}{J}\left(\frac{\partial}{\partial \xi}\alpha_{\xi x} + \frac{\partial}{\partial \eta}\alpha_{\eta x} + \frac{\partial}{\partial \zeta}\alpha_{\zeta x}\right) \\
\frac{\partial}{\partial y} &= \frac{1}{J}\left(\frac{\partial}{\partial \xi}\alpha_{\xi y} + \frac{\partial}{\partial \eta}\alpha_{\eta y} + \frac{\partial}{\partial \zeta}\alpha_{\zeta y}\right) \\
\frac{\partial}{\partial z} &= \frac{1}{J}\left(\frac{\partial}{\partial \xi}\alpha_{\xi z} + \frac{\partial}{\partial \eta}\alpha_{\eta z} + \frac{\partial}{\partial \zeta}\alpha_{\zeta z}\right)
\end{aligned} \tag{10}$$

where $\alpha_{()}$ are the partial differentials between the two coordinates and J is the Jacobian.

3.3 LES Simulations

This section presents results from numerical simulations with the wind tunnel. Numerical results are compared with the wind tunnel measurements [6] carried out at the LM wind tunnel.

3.3.a Computational Mesh

The LM Wind Power wind tunnel has the actual test section dimensions: 1.35 m in width, 2.70 m in height and 7 m in length. A NACA 0015 airfoil model of 0.9 m chord and 1.35 m span is placed across the tunnel. For numerical simulations, we use a similar configuration as in the experiment. As drawn in figure 10, the domain height is H = 2.70 m. A total tunnel length of 30 m is used in the simulations. The airfoil chord is 0.9 m and it is placed in the centre of the computational domain. Three different mesh configurations are used in the current study, namely M1, M2 and M3. For M1, the spanwise extension is 2% of the chord length. The reason of choosing a small span is due to the requirement of a small grid spacing in the spanwise direction. The streamwise, wall normal and spanwise mesh resolutions in terms of wall units shall be small enough to satisfy: $x^+ < 50$, $y^+ \approx 2$, $z^+ \approx 20$, as mentioned earlier. To meet these criteria, the present mesh has an off-wall cell size between 1×10^{-5} and 5×10^{-5} chords. For a span of 2% airfoil chords, the maximum grid-spacing measured in wall unites, is $x^+ < 30$, $y^+ \approx 2$, $z^+ \approx 20$ in the streamwise, wall normal and spanwise directions, respectively. Thus, the maximum x^+ is 15 times of y^+ and z^+ is 10 times of y^+. The total grid number used for M1 is 4.6×10^6. For M2, the grid spacing in x, y, z directions are kept the same as M1. However, the span is extended to 4% of the chord length. Therefore, the grid number is increased to 9.2×10^6. For M3, the span is extended to 20% of the chord length, but the number of grid points is still the same as for M1. This means that the grid size in the spanwise direction is 10 times larger in M3 as compared to M1.

In all the cases, periodic boundary conditions are used at the ends in the spanwise direction, wall boundary conditions are used on the top and bottom sides, inflow and outflow boundaries are set for inlet and outlet, respectively.

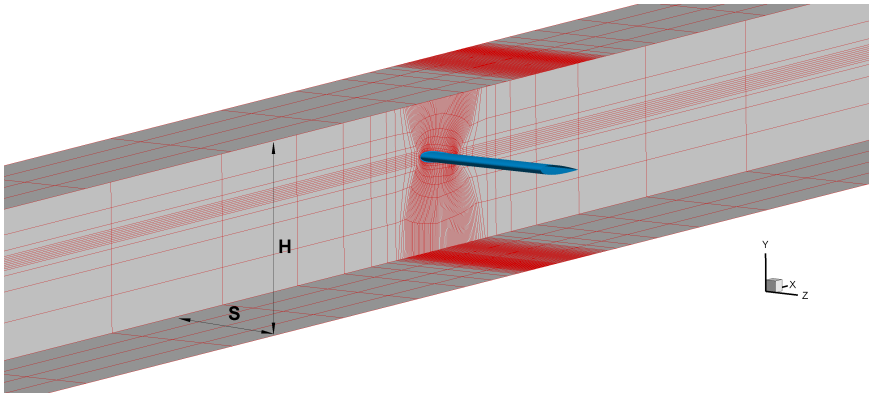

Figure 10. Mesh configuration (plotted at every 8th grid lines).

3.3.b LES Results and Comparisons

Inputs for the flow simulations on the 3 meshes are: $\Delta t = 1\times10^{-5}s$, $U_0 = 30m/s$, $\alpha = 8^o$. A snapshot of U-velocity contours is shown in figure 11. The upper and lower boundaries are the wall surfaces where velocity is zero. Flow acceleration can also be observed on the suction side of the airfoil which is up to $31m/s$. The spanwise iso-surface vorticity is plotted in figure 12 after the flow is fully established. At 8 degrees of angle of attack, the flow is near stall. Simulations on all the three meshes show that the flow separation occurs at a position not far from the leading edge on the suction side. The separation location in figure 12(c) is a bit more downstream than that in figure 12(a) and 12(b) which indicates the effect of large grid stretching in the spanwise direction. The vorticity plot consists of eddies structures of varying size, indicating the complexity of turbulent boundary layer on suction side.

At a position of x/c=0.91, the time-averaged horizontal and vertical velocity components along the line normal to the wall surface are compared with the measured data. Figure 13 shows good agreements. The computed horizontal velocity has general agreements with the experiment data. The flow is fully separated at the position x/c=0.91, the discrepancy between the simulation and the experiment indicates that a better grid resolution in streamwise direction might be needed. So far, the mean velocities obtained from M1, M2 and M3 are similar.

Time history data are recorded at several positions near the trailing edge in the wall normal direction. This allows us to compare the horizontal and vertical turbulent stresses against the hot-wire measurements. In figure 14, the turbulent stresses are plotted together along the line normal to the wall at the chordwise position of x/c=0.91. For M1 and M2, the agreements between the simulations and the measurements are satisfied, however, $< u_x u_x >$ obtained from M3 is about 2.5 times larger than those from M1 and M2. Results are also shown for the spanwise velocity component. In figure 15, the plot of turbulent stress components are plotted where $< u_z u_z >$ obtained from M3 is about 2 times larger than those from M1 and M2. As it has been noticed, even though the time-averaged velocities are similar, the velocity fluctuations in the boundary layer can be significantly different for different meshes. The present numerical study has indicated that with $\Delta z^+ \approx 200$ (M3), the results tends to 2D. In the present flow case, energy cascades

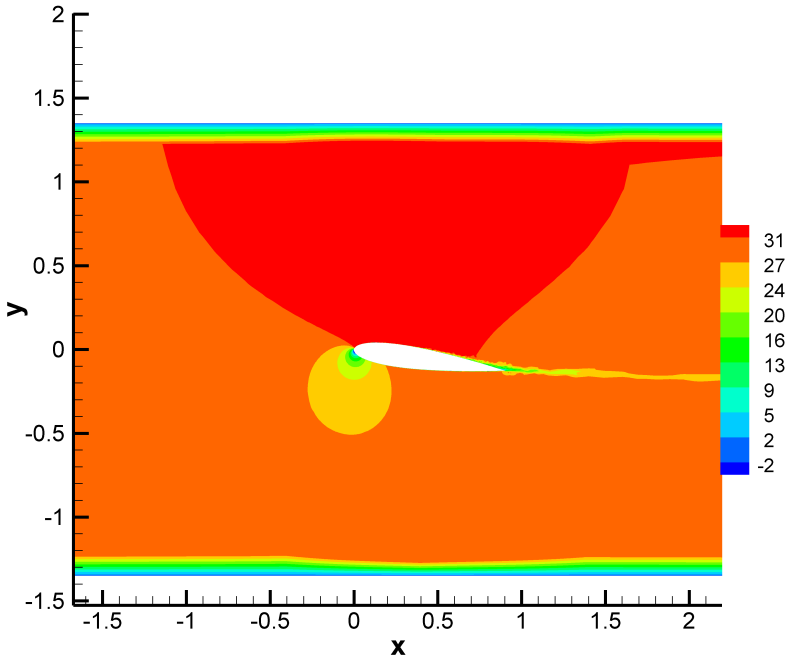

Figure 11. Horizontal velocity contour of flow past a NACA 0015 airfoil in a wind tunnel section.

from large to small eddies due to the span-wise disturbances are established such that large eddies convected from the main stream are disturbed, and small eddies are generated with energy received from larger eddies. For an over stretched grid in the span-wise direction, flow along the span are highly smoothed due to the inherent filtering effect of the SGS modeling.

To study the coherence of two signals, say, $S_1(f)$ and $S_2(f)$, the function is given by

$$Coh_{12}(f) = |S_{12}|^2 / S_1(f) S_2(f) \leq 1 \tag{11}$$

where $S_1(f)$ and $S_2(f)$ are the spectral density of two signals, $S_{12}(f)$ is the cross spectral density between two signals. Signals are linearly dependent if the coherence is 1, and it becomes zero when they are statistically independent, such that they are non-coherent. The coherence of pressure and streamwise velocity is calculated and results are shown in figure 16. It can be seen that the two signals are coherent at the four tested boundary layer positions. At high frequencies, they are less coherent because of strong numerical dissipations and under-resolved small eddies. Similar tendency can be found from the phase difference of the two signals by using equation (12).

$$\Delta\phi_{12}(f) = \arctan[Im(S_{12}(f))/Re(S_{12}(f))] \tag{12}$$

The integral time scale can be calculated as

$$R_{ij}(\tau) = \lim_{T\to\infty} \frac{1}{2T} \int_{-T}^{T} u_i(t) u_i(t+\tau) dt \tag{13}$$

For a finite number of LES data, we have

$$R_{ij}(m) = \frac{1}{N} \sum_{n=1}^{N-m+1} u_i(n) u_i(n+m-1) dt \tag{14}$$

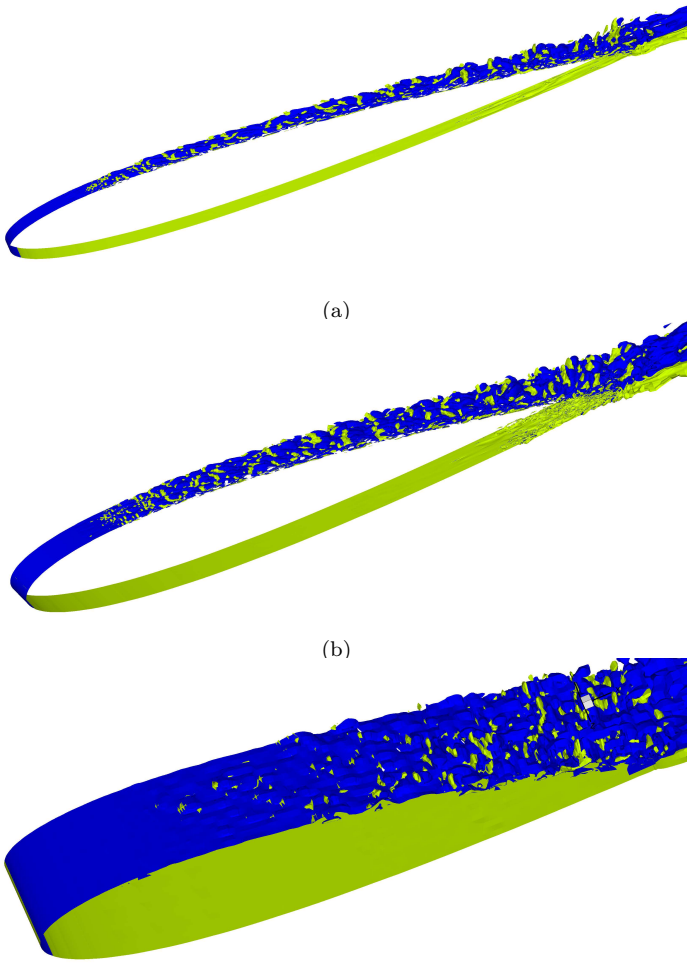

Figure 12. Instantaneous iso-surface plot of span-wise vorticity (ω_z) at a Reynolds number of 1.71×10^6 and an angle of attack of 8^o. Figures (a),(b),(c) correspond to the results computed on M1, M2 and M3, respectively.

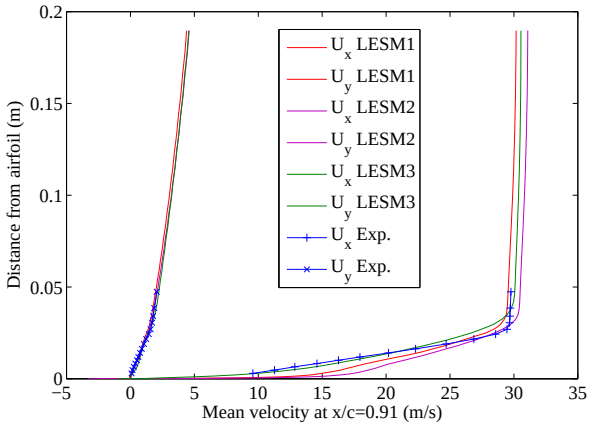

Figure 13. Mean velocities along the line normal to the wall surface.

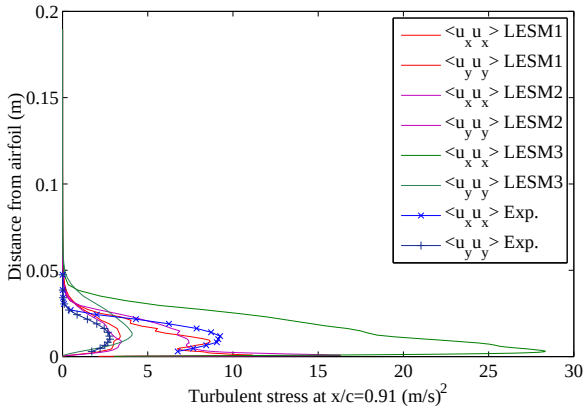

Figure 14. Turbulent stresses compared with experiments.

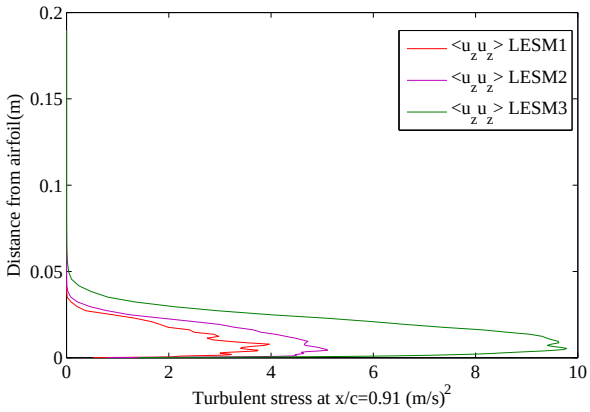

Figure 15. Span-wise turbulent stress.

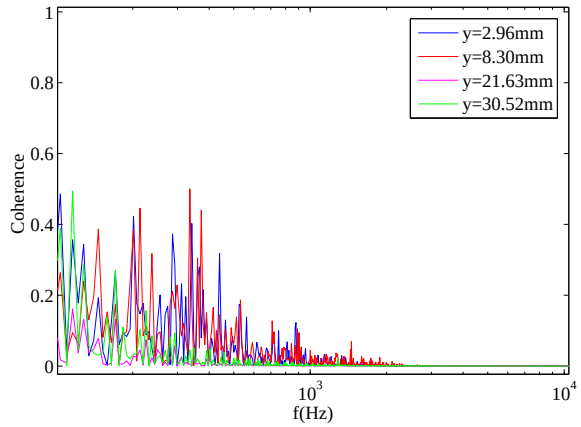

Figure 16. Coherence of pressure and streamwise velocity.

The first cross-point at zero y-axis corresponds to an integral time scale. As seen in figure 17, the time scale increases as the boundary layer thickness increases where the wave-length becomes longer.

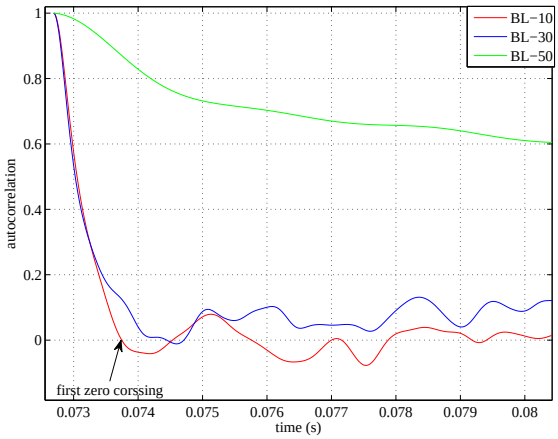

Figure 17. Autocorrelation at BL sample positions with 10%, 30% *and* 50% *of the boundary layer thickness.*

Multiplying the integral time scale by the mean velocity gives the integral length scale. The integral length scales are compared with experiment. In figure 18, the solid lines are the length scales in the mean flow direction, and the dot lines are the length scales in the cross flow direction. Again, the LES data have general agreements with the experimental data except for the case using M3.

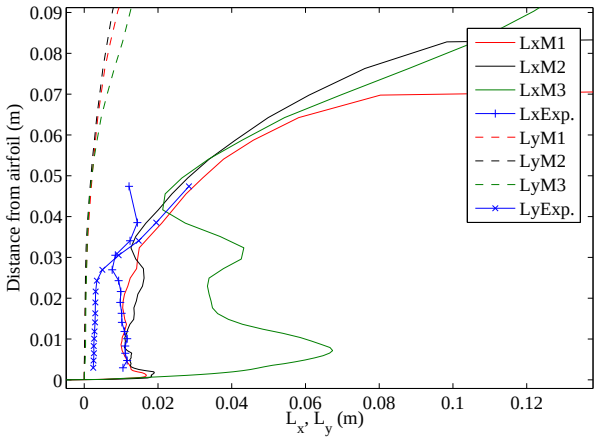

Figure 18. Turbulence integral length scales.

3.4 Conclusions

Numerical simulations have been carried out for turbulent flows over a NACA 0015 airfoil. The incompressible Navier-Stokes equations are solved by using LES with a suitable SGS turbulence model. Simulations have been compared with wind tunnel

measurements. Results have shown general agreements between simulations and experiments. Deep investigations have been performed with the aim of studying the effects of the spanwise grid size. It turns out that too large Δz leads to two-dimensional flows, where the spanwise velocity disturbances are poorly modelled.

4 Improved Trailing Edge Noise Model

Author: F. Bertagnolio

The modeling of the surface pressure spectrum under a turbulent boundary layer is investigated in the presence of an adverse pressure gradient along the flow direction. It is shown that discrepancies between measurements and results from a well-known model increase as the pressure gradient increases. This model is modified by introducing anisotropy in the definition of the vertical velocity component spectrum across the boundary layer. The degree of anisotropy is directly related to the strength of the pressure gradient. It is shown that by appropriately normalizing the pressure gradient and by tuning the anisotropy factor, experimental results can be closely reproduced by the modified model.

In this section, the original TNO-Blake model [10, 51, 48] is modified in order to account for the effects of a pressure gradient through turbulence anisotropy. The model results are compared with measurements of the surface pressure fluctuations on an airfoil section.

For more details about this study, the reader is referred to the following conference proceedings [7] or journal article [9].

4.1 Surface Pressure Model

In this section the so-called TNO-Blake model for the boundary layer surface pressure (SP) spectrum is reminded. A first correction of the model is proposed. It is then shown that the model results however still exhibit discrepancies with experimental data, and that these can be related to the presence of a pressure gradient.

4.1.a Original TNO-Blake model

Let consider a turbulent boundary layer flow over a flat plate. The direction of the flow is x_1. The direction normal to the wall is x_2 (also denoted as y in the following), and x_3 is the direction transversal to the flow. Taking the divergence of the Navier-Stokes equations for the turbulent fluctuations yields an elliptic equation for the turbulent pressure fluctuations. Assuming homogeneity in time and in the plane parallel to the surface, a one-dimensional 2^{nd} order differential equation along y for the Fourier transform of the pressure can be formulated [49]. Neglecting second order moments and using Green's function formalism, a solution for the wavenumber-frequency SP spectrum is obtained as an integral across the BL [10]:

$$\Phi_p(\boldsymbol{k}_\parallel,\omega) = 4\,\rho_0^2\,k_1^2/\left(k_1^2+k_3^2\right)\int_0^{\delta_{\mathrm{BL}}} L_2(y)(\partial U_1/\partial y)^2\,\overline{u_2^2}(y)\,\widetilde{\Phi}_{22}(\boldsymbol{k}_\parallel,\Lambda) \times \Phi_m(\omega-U_c(y)k_1)\,\mathrm{e}^{-2\,k_\parallel y}\,\mathrm{d}y \quad (15)$$

where δ_{BL} is the BL thickness, L_2 is the vertical correlation length characterizing the vertical extent of the vertical turbulent velocity component u_2, $\overline{u_2^2}$ its mean squared value, U_1 is the streamwise mean velocity, $k_\parallel$ is the norm of the wavenumber vector $\boldsymbol{k}_\parallel = (k_1, k_3)$ spanning the plane parallel to the wall, $\widetilde{\Phi}_{22}$ is the normalized spectrum of the vertical velocity fluctuations integrated over k_2, Φ_m is the so-called moving axis spectrum which describes how $\widetilde{\Phi}_{22}$ is distorted by the generation and destruction of eddies during their convection past the trailing edge (Details of its definition can be found in the paper by Moriarty [48]). The convec-

tion velocity U_c of these eddies is related to the local velocity as: $U_c(y) = 0.7\,U_1(y)$. Note that $\widetilde{\Phi}_{22}$ depends on the integral length scale Λ (see definition below) and is therefore also a function of y.

The various quantities in the integral in Eq. (15) need to be quantified in order to evaluate the SP spectrum. In this work, a Reynolds Averaged Navier-Stokes (RANS) solver is used. It directly provides the BL thickness and the mean velocity profile. The turbulent normal stress can be estimated from the turbulent kinetic energy (TKE) k_T calculated by the solver as: $\overline{u_2^2} = \alpha_k\, k_T$ where α_k is set to 0.45 or 0.3 on the suction or on the pressure side of the airfoil, respectively.

Assuming isotropy and using the classical Von Karman model, the vertical velocity spectral tensor $\widetilde{\Phi}_{22}$ reads:

$$\widetilde{\Phi}_{22}(\boldsymbol{k}_{\parallel}, \Lambda) = (4/9\pi)\,\Lambda^2\big[(\Lambda k_1)^2 + (\Lambda k_3)^2\big]/\big[1 + (\Lambda k_1)^2 + (\Lambda k_3)^2\big]^{7/3} \tag{16}$$

where the integral length scale Λ characterizes the size of the energy-containing eddies.

It can also be shown [41] that the correlation length L_2 is related to the integral length scale by:

$$L_2 = 0.7468\,\Lambda$$

In addition using the turbulence dissipation rate ϵ calculated by the RANS solver, the integral length scale can be deduced [37] from the asymptotic behavior of the Von Karman spectrum in the inertial range as:

$$\Lambda = 0.519\, k_T^{3/2}/\epsilon \tag{17}$$

The SP frequency-spectrum can be obtained by integrating Eq. (15) over the whole wavenumber space as:

$$\Phi_p(\omega) = \iint_{-\infty}^{+\infty} \Phi_p(\boldsymbol{k}_{\parallel}, \omega)\,\mathrm{d}k_1 \mathrm{d}k_3$$

As for the far-field noise radiated at the trailing edge, using the assumptions of Brooks and Hodgson [12], it results in:

$$S(\omega) = \frac{L}{4\,\pi R_2} \iint_{-\infty}^{+\infty} \frac{\omega}{c_0 k_1} \Phi_p(k_1, k_3 = 0, \omega)\,\mathrm{d}k_1$$

where L is the span length of the considered airfoil, R is the distance between the trailing edge and the observer located above the trailing edge and c_0 is the speed of sound.

4.1.b Comparison of Original Model with Measurements

In this section, the model described above is compared with surface pressure measurements on an airfoil placed in a wind tunnel. Further details on the experimental set-up are given in Section 2.1.

During this experiment, the airfoil was tested at several wind speeds (U_∞ = 30, 40, 50 m/s) and at various angles of attack (α = 0, 4, 8, 12^o). The measured SP spectra on the suction side are compared to the original model in Fig. 19. As it can be seen, there exists an offset between the measured and the modeled spectra. In addition, this offset is consistently increasing as the angle of attack increases.

It is well-known that the adverse pressure gradient developing in the BL on the suction side of an airfoil is increasing as the angle of attack increases, as long as the BL remains attached which is the case here. This suggests that the discrepancies observed above are a consequence of the model being unable to account for the influence of the pressure gradient.

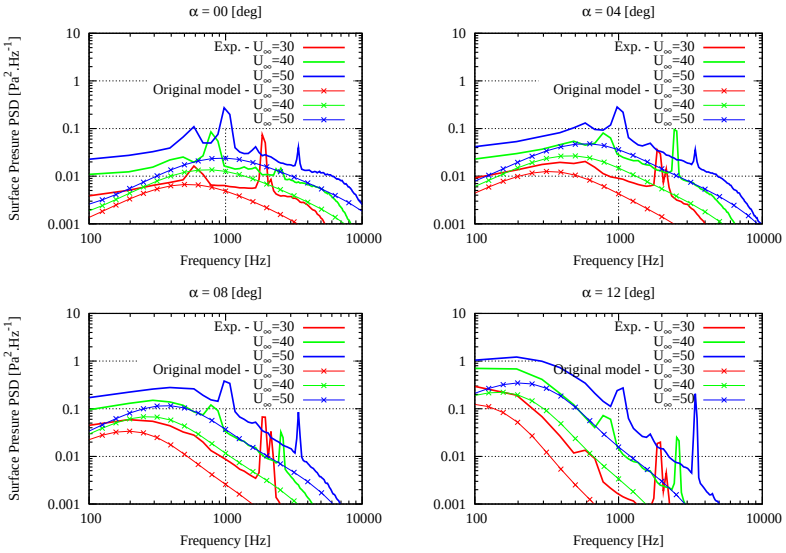

Figure 19. Surface Pressure Spectra - Comparison Experiment vs. Original Model

4.2 A New Model Including Anisotropy and Pressure Gradient

Modifications to the model are proposed in order to remedy for the discrepancies observed above. The isotropy assumption used various times to derive Eq. (15) is certainly not justified in the context of a turbulent BL flow. In addition, it has been suggested in previous work [49] that turbulence and its anisotropic characteristics can be influenced by the strength of the pressure gradient. It is here proposed to directly relate the strength of the pressure gradient to some measure of the anisotropy.

4.2.a Revisiting the Isotropy Hypothesis

Anisotropy is modeled following the approach of Panton and Linebarger [49] for which anisotropy scaling factors are introduced in order to stretch the correlation length scales along the different space directions. Starting from the original vertical velocity wavenumber spectrum derived from the Von Karman theory, the modified spectrum is stated as:

$$\widetilde{\widetilde{\Phi}}_{22}(k_1,k_2,k_3,\Lambda) = \beta_2\,\beta_3\,\frac{\Gamma(17/6)}{\pi^{3/2}\,\Gamma(1/3)}\,\Lambda^5\,\frac{[(\Lambda k_1)^2+(\beta_3\Lambda k_3)^2]^2}{[1+((\Lambda k_1)^2+(\beta_2\Lambda k_2)^2+(\beta_3\Lambda k_3))^2]^{17/6}} \tag{18}$$

where the coefficients β_2 and β_3 are anisotropy streching factors in the vertical and transversal directions, respectively. Note that this spectrum is normalized. Integrating over k_2 yields the spectrum to be used in Eq. (15):

$$\widetilde{\Phi}_{22}(\boldsymbol{k}_{\|},\Lambda) = \beta_3\frac{4}{9\pi}\,\Lambda^2\,\frac{(\Lambda k_1)^2+(\beta_3\Lambda k_3)^2}{[1+(\Lambda k_1)^2+(\beta_3\Lambda k_3)^2]^{7/3}}$$

The influence of the previous streching parameters may also be incorporated in the definition of the correlation length scale L_2 following the approach by Lynch *et al* [38]. The correlation length scale is assumed to be frequency-dependent. Assuming frozen turbulence, it can be related to the definition of the wavenumber spectrum of Eq. (18) as:

$$2\,L_2(\omega)\,\widehat{\Phi}_{22}(\omega) = 2\pi/U_c\int_{-\infty}^{+\infty}\widetilde{\widetilde{\Phi}}_{22}(k_1=k_c,k_2=0,k_3,\Lambda)\,\mathrm{d}k_3$$

where $k_c = \omega/U_c$ is the convective wavenumber. Using Eq. (18) and integrating over k_3 yields:

$$2\,L_2(\omega)\,\widehat{\Phi}_{22}(\omega) = \beta_2\,\frac{\Lambda^2}{9\pi U_c}\,\frac{3+11(\Lambda k_c)^2}{(1+(\Lambda k_c)^2)^{7/3}}$$

The frequency spectrum of the vertical velocity $\widehat{\Phi}_{22}(\omega)$ is defined as [38]:

$$\widehat{\Phi}_{22}(\omega) = 1/U_c \iint_{-\infty}^{+\infty} \widetilde{\widetilde{\Phi}}_{22}(k_1 = k_c, k_2, k_3, \Lambda)\,\mathrm{d}k_2\,\mathrm{d}k_3$$

Introducing again Eq. (18) and integrating over the k_2-k_3 space yields:

$$\widehat{\Phi}_{22}(\omega) = \frac{6\,\Gamma(17/6)}{55\,\sqrt{\pi}\,\Gamma(1/3)}\,\frac{\Lambda}{U_c}\,\frac{3+8(\Lambda k_c)^2}{(1+(\Lambda k_c)^2)^{11/6}}$$

Combining the previous results provides an estimate for the correlation length scale:

$$\frac{L_2(\omega)}{\Lambda} = \beta_2 \frac{55\,\Gamma(1/3)}{108\,\sqrt{\pi}\,\Gamma(17/6)}\,\frac{3+11(\Lambda k_c)^2}{3+8(\Lambda k_c)^2}\,\frac{1}{\sqrt{1+(\Lambda k_c)^2}} \tag{19}$$

In the present implementation of the model, Eq. (17) is still used to evaluate the integral length scale Λ from the TKE and its dissipation rate calculated by the RANS solver.

4.2.b Pressure Gradient Scaling

Various scalings have been proposed in the past for obtaining self-similar BL profiles in the presence of a pressure gradient (see [2] for a review). However, to the best author's knowledge, there is no such scaling that is designed for turbulence spectral analysis. In our case, the following non-dimensional pressure gradient is introduced:

$$\gamma = (\delta^*/U_\mathrm{e})\left((\partial P/\partial x_1)^2/\rho\,\mu\right)^{1/3}$$

where δ^* is the displacement thickness, μ is the dynamic viscosity, U_e is the mean velocity at the edge of the BL, and P the mean pressure. In this work, the mean pressure gradient is evaluated from the mean surface pressure using the RANS calculations. It is expected to be a good approximation of the pressure gradient across the BL as the pressure gradient normal to the surface should be roughly constant across the BL according to turbulent BL theory.

The anisotropy factors that were introduced above to modify the vertical velocity spectrum are now defined as functions of γ as:

$$\beta_2 = \beta_3 = (20\,\gamma)^{2/5}$$

The above formula is purely empirical and was tuned so that model results best fit the measurement data presented in the next section. It is important to note that this formula would become inconsistent for a zero-pressure gradient BL as the factors would cancel. A more advanced formula should then be devised in order to make the model more general.

4.3 Analysis of Results

The new model defined above is now applied to the case of an airfoil that is tested in a wind tunnel and for which surface pressure is measured.

4.3.a Wind-Tunnel Measurements

The LM Wind Power wind tunnel is designed for the testing of wind turbine airfoils. The actual test section dimensions are 1.35 m in width, 2.70 m in height,

and 7 m in length. A NACA0015 airfoil section with a chord $C = 0.9$ m is placed across the width of the tunnel. During this study, three inflow velocities are investigated: $U_\infty = 30$, 40 and 50 m/s, as well as four angles of attack: $\alpha = 0$, 4, 8 and 12^o. Assuming an average air temperature of 23^oC in the wind tunnel, the corresponding Reynolds numbers for the airfoil flow are $Re = 1.7$, 2.3, 2.85×10^6. In the results presented here, no BL turbulence triggering device is present on the airfoil surface.

High-frequency microphones are flushed-mounted beneath the surface of the airfoil. The microphone considered in this work is located at $x/C = 0.894$. All details about this experiment can be found in [6, 24].

4.3.b Navier-Stokes Solver

The RANS solver used for the fluid flow calculation is the in-house code EllipSys2D [64]. It solves the incompressible Navier-Stokes equation on a structured mesh in a predictor-corrector fashion using the classical SIMPLE algorithm. Turbulence is modeled using the k-ω SST model by Menter [43]. In all the calculations presented in this paper, the transition is set free and the e^n transition model ($N_{\text{crit}} = 9$) by Drela and Giles [22] is used.

4.3.c Results Comparisons

The model described above involves anisotropy factors $\beta_2 = \beta_3$. This factor is evaluated from RANS calculations and is plotted in Fig. 20(b) as a function of the angle of attack for the 3 experimental inflow velocities, next to the pressure gradient in Fig. 20(a). As it can be seen, the anisotropy factor increases almost linearly with angle of attack and it is nearly insensitive to the inflow velocity contrary to the pressure gradient.

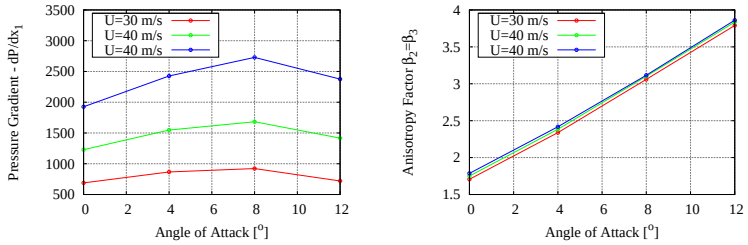

(a) Pressure Gradient (b) Anisotropy Factor

Figure 20. Modified Model Parameters

The SP spectra obtained with the modified model for the different inflow conditions and angles of attack are displayed in Fig. 21. This figure has to be compared with the original model results in Fig. 19. The modified model results are now in good agreement with the measurements irrespectively of the experimental conditions. Some discrepancies can still be observed in the low-frequency range. However, the TNO-Blake model is eventually no more valid in the low-frequency limit.

4.4 Conclusions

A modified version of the TNO-Blake model was proposed in order to account for the effect of adverse pressure gradient in an airfoil BL, as well as the subsequent turbulence anisotropy. The model proved to improve the SP spectrum predictions when compared to wind tunnel measurements.

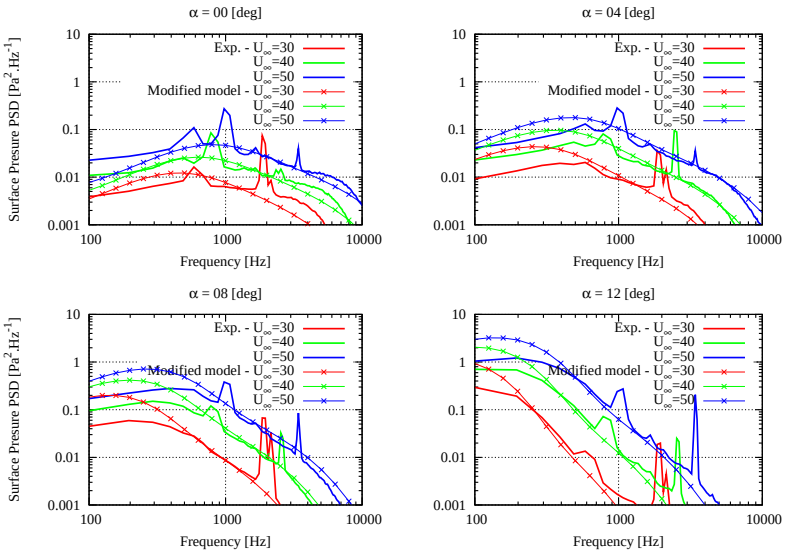

Figure 21. Surface Pressure Spectra - Comparison Experiment vs. Modified Model

However, it must be kept in mind that the proposed model was tuned for the above-mentioned experimental results. Further study must be conducted to verify that the model is general and can be applied to different airfoil types or experimental conditions.

5 Noise Evaluation Technique Based on Surface Pressure

Author: A. Fischer

In this chapter the relevant theory for the understanding of TE noise modeling is collected. It contains the acoustic formulations of [31] and [57]. Both give a relation for the far field sound pressure in dependence of the frequency wave number spectral density of the pressure on the airfoil surface.

5.1 Theory

The first attempt to model trailing edge (TE) noise analytically was done by Ffwocs Williams and Hall [70] in 1970. They applied Lighthill's acoustic analogy to flow on a semi-infinite half plane and determined the radiation in terms of the assumed velocity field. Chase [14] developed a theory to relate the sound field to the surface pressure fluctuations on the surface close to the TE of the airfoil. His approach was refined by Chandiramani [13] and some years later Howe [31] unified the TE noise theory and generalized Chase's [14] and Chandiramani's [13] theory. He showed that the model can be directly derived from Lighthill's acoustic analogy.

Amiet [1] developed a theory based one a similar approach as Chase [14], but with a different response function from the airfoil. His theory was recently revised by Roger [57]. In the present work Howe's formulation and Amiet's model with Roger's extension are applied. The model formulations is briefly repeated below.

5.1.a Howe's Relation Between Far-Field Noise and Surface Pressure Spectrum

Using Lighthill's acoustic analogy recast in term of the stagnation enthalpy instead of the pressure as primary acoustic variable and making a number of hypothesis, Howe [31] find a solution for the scattering phenomenon at the trailing edge of a flat plate through a relationship between the SP spectrum and the far-field noise:

$$S_f(\omega) = \frac{2LM_c}{\pi R^2} \frac{\sin\Phi \sin^2(\Theta/2)\cos\alpha}{(1+M_{0R})^2(1-M_{WR})^2} \frac{\Pi_s(\omega/U_c, (\omega/c_0)\cos\Phi)}{(1-M_c\vec{n}\cdot\vec{r})^2(1-M_c\sin\Phi)} \qquad (20)$$

where L is the plate span length, U_c the convective velocity and M_c the convective Mach number, R is the distance to the observer, $M_{0R} = M_0(x_1/R)$ is the component of the free stream Mach number in the observer direction, c_0 is the speed of sound. $\vec{n} = (\cos\alpha, \sin\alpha)$ is the unit vector in the direction of the mean boundary layer/eddy convection velocity and $\vec{r} = (\sin\Phi\cos\Theta, \cos\Phi)$ is the unit vector in the observer direction. The geometric angles α, Θ and Φ are defined in the sketch in Fig. 22. In the previous equation $\Pi_s(K_1, \omega)$ is the SP spectrum near the trailing edge.

5.1.b Amiet's Model with Roger's Extension

Amiet [1] assumes in his model that the turbulent flow convecting over the airfoil produces a convective pressure pattern on the surface of the airfoil. The convective pressure pattern creates a radiating pressure field near the TE of the airfoil. The radiation of sound to the far field is then solved with a Schwartzschild technique. The approach of Amiet assumes a 2D setup and an infinite chord length. Roger [57] extends Amiet's model to be valid for a 3D flow field and corrects for a finite chord length.

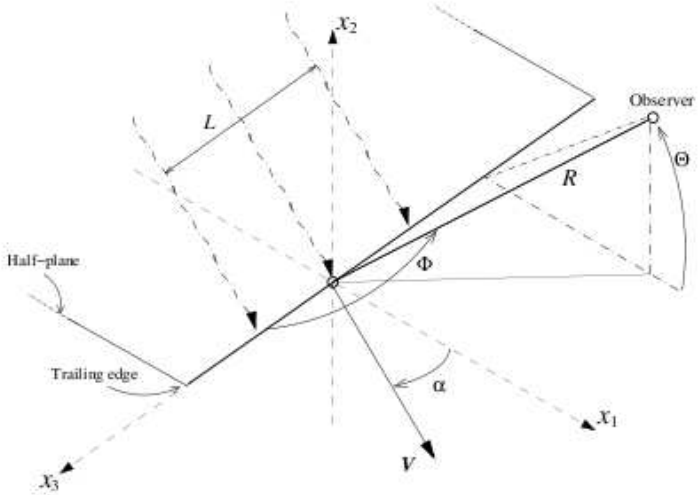

Figure 22. Half-plane Configuration

The final result for the above analysis is the following:

$$S_f(\vec{y},\omega) = \left(\frac{\omega y_2 b}{2\pi c_0 S_0^2}\right)^2 2\pi L \left| I\left(\frac{\overline{\omega}}{U_c}, \overline{K}_3\right)\right|^2 \Pi_0\left(\frac{\omega}{U_c}, k_0\frac{y_3}{S_0}\right) \tag{21}$$

where I is a radiation integral whose definition can be found in the reference [57]. Now the function Π_0 can be related to the one-point SP spectrum $\Phi_{pp}(\omega)$ and the spanwise correlation length as:

$$\Pi_0\left(\frac{\omega}{U_c}, k_0\frac{y_3}{S_0}\right) = \frac{1}{\pi}\Phi_{pp}(\omega) l_3(k_0\frac{y_3}{S_0}, \omega) \tag{22}$$

The both last quantities can be measured in a wind tunnel using surface microphones. The use of these microphones for surface pressure measurements are described in the next section.

5.2 Surface Pressure Measurements

The fluctuating pressure on an airfoil surface is very sensitive to small changes of the surface. Microphones have to be mounted in way which creates the smallest possible disturbance of the surface. This was realized by mounting microphones inside the airfoil and connecting them via a pinhole with the surface. This configuration has the additional advantage that the sensitive area of the sensor on the surface is minimized and its spacial extend is smaller than a typical eddy size at the highest frequency of interest. If the typical eddy size becomes smaller than the sensitive area of the sensor, the signal is attenuated. Corcos [16] is the earliest work trying to resolve this problem and gives a semi-empirical correction for the attenuation of the signal. However, if the surface pressure fluctuations should be determined with low uncertainty, it should not be necessary to apply this correction.

The microphones used in the present experiments were back-electret condenser microphones of Sennheiser type KE4-211-2. A microphone housing which can be integrated in the airfoil surface was developed by Madsen *et al* [39]. The geometry of this housing and the Sennheiser microphone is displayed in Fig. 23.

The design goal for the housing was to have the Helmholtz eigen-frequency of the air in the cavity between pinhole opening and microphone above 10 kHz. However, the Helmholtz eigen frequency shifted strongly with small changes in

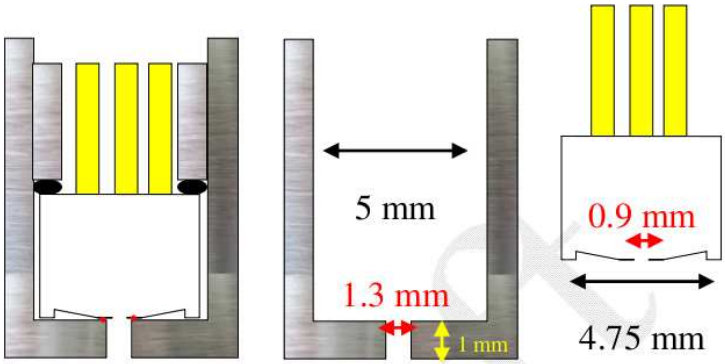

Figure 23. The Sennheiser KE4-211-2 Condenser Microphone and its Housing (from [27])

the housing geometry and/or the mounting torque. For accurate measurements the pinhole microphone have to be calibrated when mounted, as outlined below. In the Virginia tech experiment the microphones were directly mounted in the airfoil model without using the housing, if the space inside the airfoil allowed. They were calibrated individually when mounted.

The mounting space close to the trailing edge of the airfoil models was very small. To access these locations the microphones had to be connected to the pinhole via a tubing system. The first generation of the microphone adapter with tubing system is illustrated in Fig. 24.

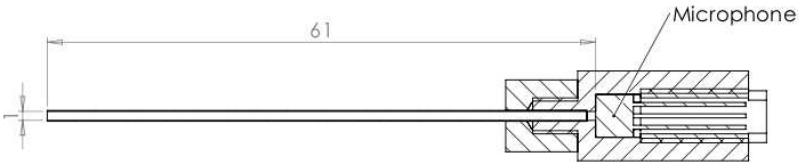

Figure 24. The First Generation of the Microphone Adapter with Tubing System

It was used in the NACA0015 airfoil model. The reflection in the tubing system created an interference pattern in the transfer function between the pressure at the pinhole and the pressure at the microphone. A second generation of the tubing system which did not suffer from the flaws was developed. It was copied from the design of [52]. This microphone adapter is used in the NACA 64-618 and the NACA 64-618$_{\mathrm{T}}$ model. The main change of the second design compared to the first is the continuation of the tubing system with a 2 meter long plastic tube with internal radius of 3 mm downstream of the microphone position. Interference patterns are less strong, because the reflected sound wave is attenuated.

5.2.a Analytical Modeling of the Pinhole Microphones

An analytic model to describe the transfer function between the pressure at the pinhole and at the microphone location was developed. The analytical model corresponding to the microphones mounted directly in the airfoil and mounted in the housing of Fig. 23 is the one of a Helmholtz resonator. The transfer function between microphone and source pressure of the Helmholtz resonator model is given by [42]. All details about this model used subsequently for SP calibration are given

in the thesis by A. Fischer [23].

5.2.b Calibration of the Surface Pressure Microphones

The calibration method for the NACA0015 is described in [24]. The calibration function we found by this method was contradictory to the one found by Brüel & Kjær [27]. The calibration setup of Guastavino [27] is considered more accurate, because the signal to noise ratio is improved by several orders of magnitude compared to the old one. Hence, it was decided not to use the calibration functions found by [24] andt the calibration method of [27] was developed for the Virginia Tech Wind Tunnel experiment. The Brüel & Kjær Probe Microphone Type 4182 with a 50 mm probe was used a reference. It was placed as close as possible to the pinhole (see Fig. 25(a)). A Sennheiser headphone HD650 was used as source for

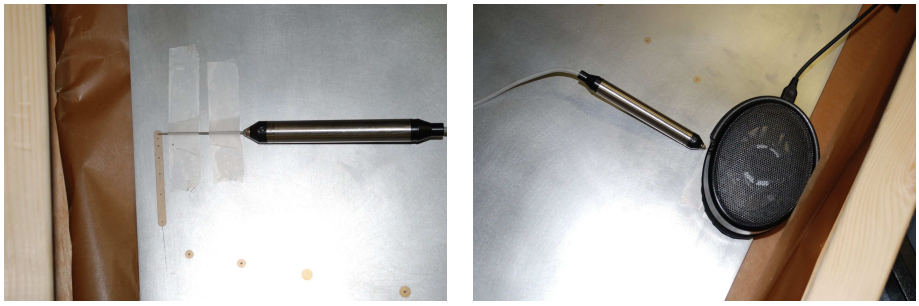

(a) Reference Microphone and Pinhole (b) Sennheiser Headphone HD650 Source

Figure 25. Calibration Setup of the Surface Pressure Microphones in VT Experiment

the calibration (see Fig. 25(b)). A B&K PULSE Data Acquisition Hardware Type 3560-B-130 together with the PULSE LabShop v. 15.1.0.15 Software was used for data acquisition and source feeding. The high frequency compensation for the B&K Probe Microphone Type 4182 with a 50 mm probe was implemented in the PulseLab software. The calibration signal was a sweep in 1/48th octave bands with center frequencies from 16 to 50 Hz. An individual calibration function for microphone 10 to 24 as well as microphone 28 and 29 was obtained. The calibration was performed in a laboratory at Virginia Tech University. The ambient temperature, pressure and humidity were recorded.

5.2.c Discussion of Measured and Analytic Transfer Functions

Figure 26 shows the transfer function of microphone no. 10, 12, 14 and 15 on the NACA 64-618 airfoil. Those microphones were mounted directly on the airfoil. To compute the transfer in dB the Sennheiser microphone electric signals were multiplied with a fictive sensitivity of 10 mV/Pa (manufacturer value). A considerable scatter in the transfer function of the different microphones is observed. This points out the importance of individually calibrating the microphones after mounting. The transfer functions have the typical shape of the Helmholtz transfer function, but the eigen-frequency and the damping coefficient are very different compared to the ones of the configuration microphone and housing as in Fig. 23.

Figure 27 shows the transfer function of microphone no. 17, 19, 24 and 28 on the NACA 64-618 airfoil. All of them are placed in a tube adapter. The scatter is less the for the directly mounted microphones, expect for frequencies above 7 kHz. It exhibits a strong interference pattern in the frequency range below 1 kHz. This is due to reflexions at the end of the plastic tube. In further applications, a longer and thinner (to increase the damping coefficient) plastic tube should be used.

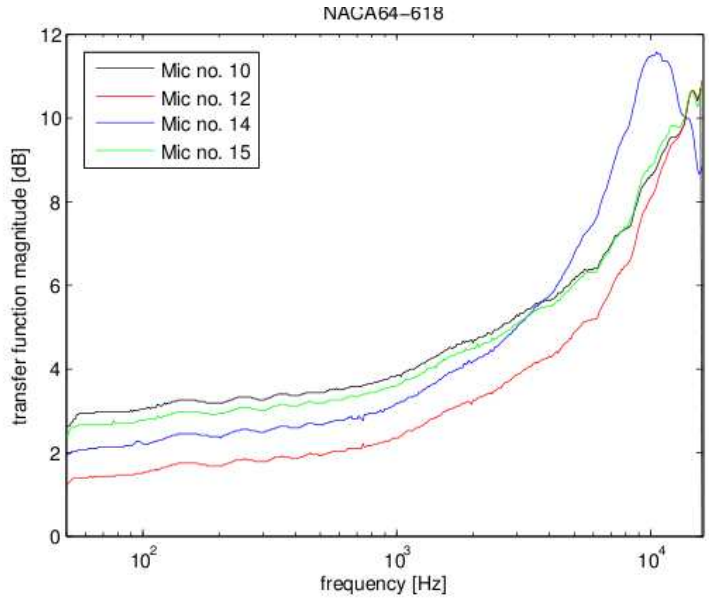

Figure 26. Transfer Function between Microphone and Source Pressure as Function of Frequency

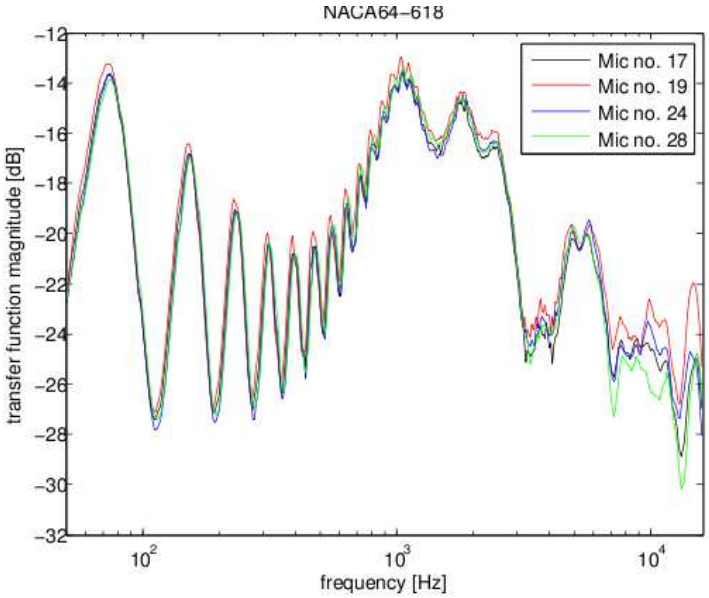

Figure 27. Transfer Function between Microphone and Source Pressure as Function of Frequency

6 Noise Optimized Airfoil Design

Author: F. Bertagnolio

The optimization of airfoil profiles specifically designed for wind turbine application was initiated in the late 80's [67, 68, 30, 15]. The first attempts to reduce airfoil noise for wind turbines made use of airfoil trailing edge serration [32, 18, 11]. The modification of airfoil shapes targeted at noise reduction is more recent [28, 29]. An important effort was produced in this direction within the SIROCCO project [59]. This latter work involved measurements on full size wind turbines and showed that trailing edge serration may proved a viable solution for mitigating wind turbine noise though it has not been implemented on commercial wind turbine yet. It should be mentioned here that the attenuation of turbulent inflow noise using wavy leading edge has recently been investigated [55], but this technique has still to be further validated for practical applications.

In this paper, it is proposed to optimize an airfoil which is used for wind turbine applications, namely the NACA 64-618 airfoil. The optimization procedure is performed with the in-house code AirfoilOpt. The objective is to reduce trailing edge noise, preserving some of the aerodynamic and geometric characteristics of the original airfoil using constraints at the same time. In this way, the resulting airfoil should remain a realistic candidate for wind turbine applications and comparisons between the original and optimized airfoils remain fair. As for the verification in wind tunnel, the reader is referred to Section 7.3.

For more details about this study, the reader is referred to the following journal article [8].

6.1 Aerodynamic and Trailing Edge Noise Modeling

Xfoil [21] is an airfoil flow solver that couples a panel method to compute the inviscid flow around the airfoil outside the BL together with a solution method for the BL equations in order to determine its development along the airfoil chord. BL transition to turbulence can be fixed or evaluated with the e^n transition model by Drela and Giles [22]. The code can handle transitional separation bubbles and limited TE separation, as well as to a certain extent lift and drag predictions beyond maximum lift. Due to its short computational requirements, this program will be used for the optimization procedure described later.

For a preliminary validation of the design results, the CFD code EllipSys2d will be used. The Navier-Stokes incompressible flow solver EllipSys2D used for airfoil flow calculations was developed as a co-operation between the group of Aero-Elastic Design at Risø-DTU and the department of Fluid Mechanics at DTU. Both entities are now merged within DTU Wind Energy (Department of Wind Energy, Technical University of Denmark) [45, 47, 63].

It is designed to solve the 2D Navier-Stokes equations for an incompressible fluid. It uses a cell-centered grid arrangement for the pressure field and the cartesian velocity components. The equations are discretized by means of a finite volume formulation. The well-known velocity-pressure decoupling is circumvented by using the Rhie and Chow interpolation technique [56]. The PISO algorithm is used for solving the momentum and pressure equations in a predictor-corrector fashion [33]. Details about the numerical code and discretization issues can be found in the references [45, 47, 63].

The trailing edge noise model used for the noise optimization of the airfoil is the TNO model described in Section 4.1.a. Note that this is the original model

version developed by Parchen [51] since the improved model version introduced in Section 4.2 was not available yet at the time of the present study.

6.2 Airfoil Aero-Acoustic Optimization

6.2.a Optimization Program AirfoilOpt

The optimization code AirfoilOpt is an airfoil/blade section profile design tool that was developed in the group of Aero-Elastic Design at Risø-DTU [26, 25]. A gradient-based algorithm (Successive Linar Programming) is used to reduce a given cost function subject to various constraints [17]. In short, for a given set of design parameters at each iteration of the numerical procedure the code calculates the local gradients of the cost function with respect to each design parameter in order to find a new iterate improving the value of the cost function. This cost function can be a linear combination of various geometric (surface curvature, camber, thickness distribution, etc...) and/or aerodynamic (lift, drag, moment coefficients, lift-to-drag ratio, transition location, etc...) characteristics of the airfoil section. The aerodynamic data are computed with the airfoil analysis code Xfoil by Drela [21]. In addition, non-linear constraints on the geometric and aerodynamic properties of the airfoil can be enforced during the optimization process. Note that the cost function and constraints may involve aerodynamic characteristics of the airfoil calculated both using fixed transition flow conditions or with transition modelling in the flow solver. The SLP optimization algorithm is a well-tested and stable technique but it can be computationally expensive due to the large number of flow calculations required to calculate the cost function gradients. It may also fail to reach the global optimum and find instead a local optimum depending on initial conditions. In an attempt to remedy to this latter drawback, the 'move limits' technique for exploring the design space combined with a line search procedure is implemented.

The optimization code also includes TE noise as a possible component of the cost function or constraints. In this study, the maximum value of the far field sound pressure level (SPL) spectrum across the whole frequency range is used as the cost function. The integrated spectrum value may also be used but both methods give similar results. It was found in a preliminary study that A-weighting alters the convergence of the optimization algorithm by smearing out the cost function gradients. Therefore, the non-filtered spectra are only considered here. Both the pressure and the suction side noise spectra are considered and added to each other to form the cost function. However, the suction side generated noise will prevail for the flow conditions that we are interested in.

6.2.b New Airfoil Design

The reference airfoil for this study is the NACA 64-618 airfoil. This airfoil was chosen because it has been used for designing various wind turbine blades. Its characteristics are laminar flow conditions along a large part of the airfoil chord and a smooth post-stall behavior. This airfoil profile is used as the initial guess for the iterative optimization procedure described above.

Our strategy is to use as cost function the emitted TE noise (peak value or integral value across the SPL spectrum) as predicted using the TNO model together with the BL flow solver Xfoil. Note that in this case, the fixed transition case for the the flow conditions was assumed for evaluating the cost function. As it will be seen later, this has the unfortunate consequence that noise was not significantly reduced in the free transition case. The Xfoil flow calculations used to evaluate the noise SPL for the cost function (and the aerodynamic data for the constraints, see below) are all performed at a Reynolds number $Re = 1.5 \times 10^6$. The SPL used for

the cost function evaluation are evaluated at a relative angle of attack $\alpha_0 = 10^o$ which approximately corresponds to the angle of attack at maximum lift-to-drag ratio. In the fixed transition case, transition is enforced at $x/C = 5\%$ on the suction side, and 10% on the pressure side of the airfoil.

In order to preserve some of the aerodynamic and geometric characteristics of the reference airfoil, constraints are enforced on specific values of these characteristics. The value of the lift and of the lift-to-drag ratio at maximum lift-to-drag ratio angle of attack (i.e. design point set at $\alpha_0 = 10^o$) are constrained as:

$$1.0 < C_l \quad \text{and} \quad 60 < C_l/C_d \qquad \text{at} \quad \alpha_0 = 10^o$$

in the case of fixed transition calculation and:

$$1.1 < C_l \quad \text{and} \quad 140 < C_l/C_d \qquad \text{at} \quad \alpha_0 = 10^o$$

for the free transition case. In order to preserve maximum lift and a smooth stall behavior, the additional following contraints are enforced:

$$1.35 < C_l < 1.78 \quad \text{at} \quad \alpha_0 = 23^o \qquad \text{and} \qquad 1.2 < C_l \quad \text{at} \quad \alpha_0 = 28^o$$

in the fixed transition case, and for the free transition case:

$$1.38 < C_l < 1.85 \quad \text{at} \quad \alpha_0 = 23^o \qquad \text{and} \qquad 1.2 < C_l \quad \text{at} \quad \alpha_0 = 28^o$$

As for the geometric constraints, the airfoil maximum thickness is kept equal to 18% and its chord location is restricted to be located in the interval $0.35 < x/C < 0.41$. A minimum thickness of 15% is enforced in the interval $0.16 < x/C < 0.56$. In order to avoid a collapse of the TE thickness, it is limited to be higher than 2.2% for $x/C > 0.9$, 0.8% for $x/C > 0.94$, 0.4% for $x/C > 0.96$, and 0.3% for $x/C > 0.98$. The airfoil surface curvature is also monitored to keep sensible values, in particular near the leading edge.

6.3 Analysis of Xfoil/TNO Results

The aerodynamic polar characteristics of the new airfoil design resulting from the above optimization process, which is denoted as NACA 64-618$_{\mathrm{T}}$, are compared to those of the original NACA 64-618 airfoil in Figs. 28(a) and (b) for the free and fixed transition cases, respectively. Note that the lift curves are plotted as a function of the angle of attack relative to zero lift α_0. The computational results obtained with Xfoil, as within the optimization algorithm, and those obtained with the CFD code EllipSys2D, are displayed in the figures.

It can be observed that both Xfoil and the CFD code predict slightly better aerodynamic characteristics for the optimized airfoil. Indeed, this airfoil exhibits a quite larger maximum lift, though together with an increase of drag at the same maximum lift angle of attack (roughly by a factor 3.5 compared to the linear region for the free transition case, and a factor 2 for fixed transition case). The aerodynamic characteristics beyond this point (say above $\alpha_0 = 15^o$) slightly differs for the two airfoils. While the numerical codes predict a continuous increase of lift for the original airfoil along with a rapid increase of drag, the optimized airfoil presents a more abrupt stall, though with a rather smooth lift drop.

It should be noted that the CFD calculations predict slightly higher lift at all angles of attack and a somewhat different behavior around stall compared to Xfoil. However, even if the CFD code should provide a better flow approximation, in particular when flow separation occurs, the accuracy of both methods is always questionable in these conditions.

To get a general overview of the airfoils acoustic characteristics, the noise spectra are integrated from 100 to 1 kHz and plotted as a function of the lift coefficient. The results are displayed in Figs. 29(a-b) for the free and fixed transition cases,

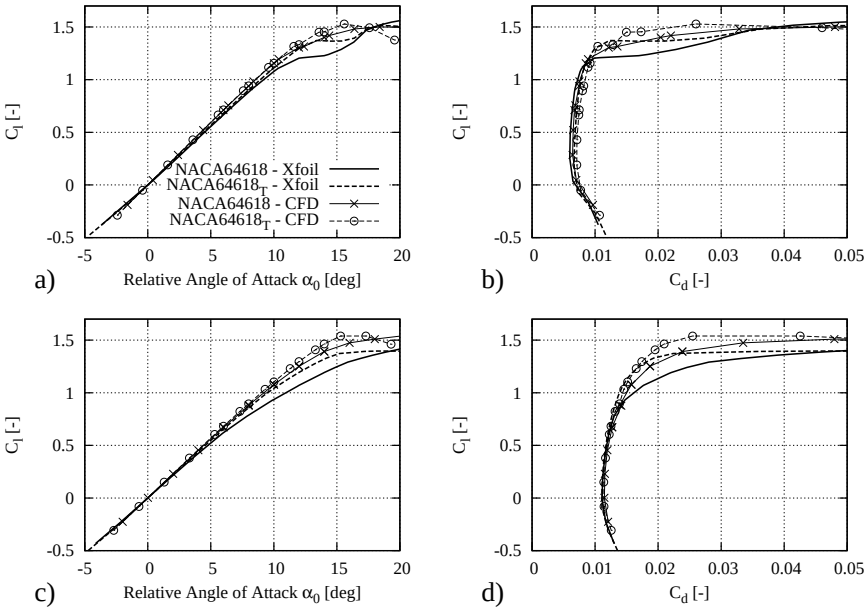

Figure 28. Aerodynamic polar characteristics, $Re = 1.5M$: a-b) Free transition, c-d) Fixed transition.

respectively. The CFD/TNO calculations shows that the original and optimized airfoils behave quite similarly at all angles of attack as far as noise is concerned, whereas Xfoil calculations confirm that noise is significantly reduced for the fixed transition case but not for free transition. In this latter case, noise is slighyly increase at lower angle of attack and decrease at higher angles for the optimized airfoil, the limit between the two tendencies being located at the design point $\alpha_0 = 10^o$ corresponding to a lift approximately equal to $C_l = 1.1$ (see Fig .28).

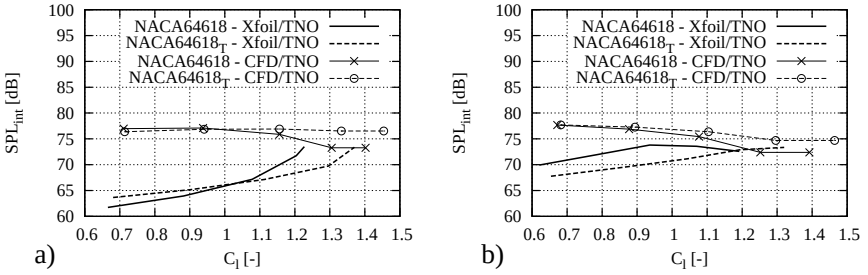

Figure 29. Integrated noise spectra (100 to 1000 Hz) using original TNO model as function of lift: a) Free transition, b) Fixed transition.

6.4 Conclusions

As a conclusion, even if some noise reductions could be achieved without compromising, or actually even slightly improving the airfoil aerodynamic characteristics, it still remain to be proved that these conclusions will hold for the actual airfoil section in a real environment. Indeed, the allegedly more accurate CFD flow solver combined with the TE noise model did exhibit almost no noise reduction. An important conclusion is therefore the fact that the Xfoil solver might not be suited to the optimization goal that was set, i.e. TE noise reduction. The failure to correctly

predict the turbulent kinetic energy in the turbulent BL, at least compared to CFD calculations, might mislead the optimization algorithm to a solution which does actually not meet the expected goals in real life. In Section 7, the actual trailing edge noise emission are evaluated through a wind tunnel experiment.

7 Wind Tunnel Measurements at Virginia Tech

Authors: A. Fischer and F. Bertagnolio

In this section, the wind tunnel configuration used for aerodynamic and aeroacoustic measurement is described. Then, the validation of the method for evaluating far-field noise from surface microphones as described in Section 5 is presented. Finally, the design concept proposed in Section 6 is verified.

7.1 Virginia Tech Stability Wind Tunnel

The Virginia Tech Stability Wind Tunnel (VTST) is a closed loop subsonic wind tunnel with a 1.83m x 1.83m rectangular removable test section (see Fig. 30).

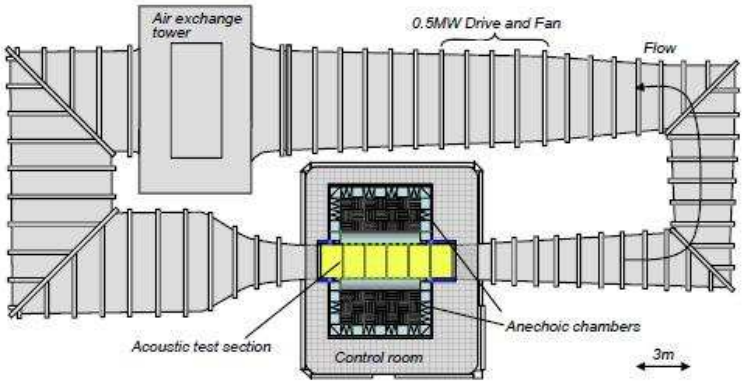

Figure 30. Schetch of the Virginia Tech Stability Wind Tunnel in acoustic configuration

The length of the test section is 7.3m. The tunnel is driven by a 0.45MW fan of 5.3m diameter. A flow speed of 75m/s can be reached with empty test section. Downstream of the fan an air exchange tower open to the atmosphere is located. From there the flow is directed into a 5.5m x 5.5m settling chamber. The settling chamber contains 7 screens with open area ration 0.6 and a separation of 0.15m. The flow enters the test section through a nozzle with contraction ratio 9:1 and leaves it through a 3 degree diffuser. All corners of the tunnel are equipped with an array of shaped turning vanes. Turbulence intensities of less than 0.05% were reported from measurements in the aerodynamic test section.

Two different test sections are available for the tunnel: a hard walled aerodynamic test section and a acoustic test section with Kevlar walls. In the present experiment the acoustic test section was used. The acoustic test section is surrounded by anechoic chambers (see Fig. 31). The Kevlar walls were designed to contain the flow and keep the same aerodynamic performance as with a closed test section while sound waves are transmitted through the walls and can be measured in the anechoic chamber.

7.1.a Airfoil Models

Two airfoil models were tested in the VTST: a NACA 64-618 and a modified version called NACA 64-618$_{\mathrm{T}}$. The airfoil models had a chord length of 0.6 m and a span of 1.82 m. They were made from a full aluminum block by RIVAL A/S in Denmark. The machining accuracy of the surface is ±0.1mm measured spanwise

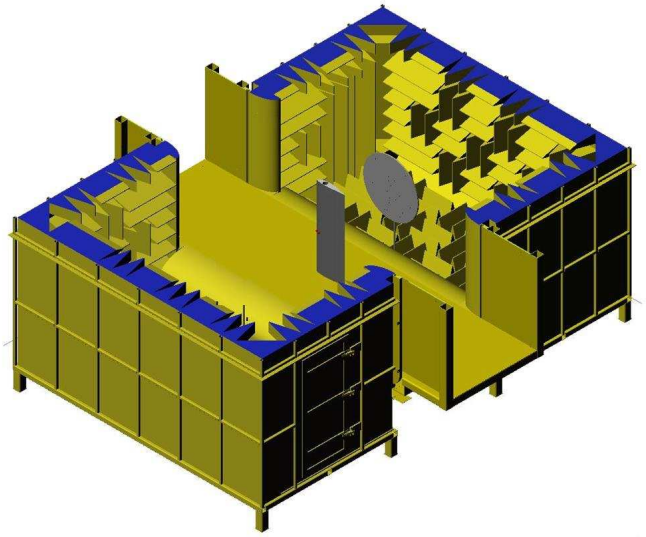

Figure 31. The acoustic test section of the VTST

from end to end. Each airfoil was equipped with 62 pressure ports (0.5 mm pinhole diameter) and 29 surface pressure microphones.

Microphones connected to a pinhole close to the trailing edge were installed with an tube adapter. The diameter of the pinhole on the surface was 1 mm. The other microphones were installed in a cavity on the airfoil surface. The pinhole diameter was 1.3 mm. Details of the microphone installation and calibration are given in Section 5.2.

Fig. 32 shows the NACA 64-618 airfoil mounted in the acoustic test section of the wind tunnel. The airfoils are flush-mounted with the wind tunnel walls. The gap between the airfoil and the tunnel wall was bridged with a transition piece made of three layers: aluminum, foam and Teflon. The Teflon layer minimizes friction when sliding over the tunnel walls while changing the angle of attack. To ensure a smooth surface at the junction, a Mylar strip was wrapped around the airfoil and transition piece and fixed with aluminum tape.

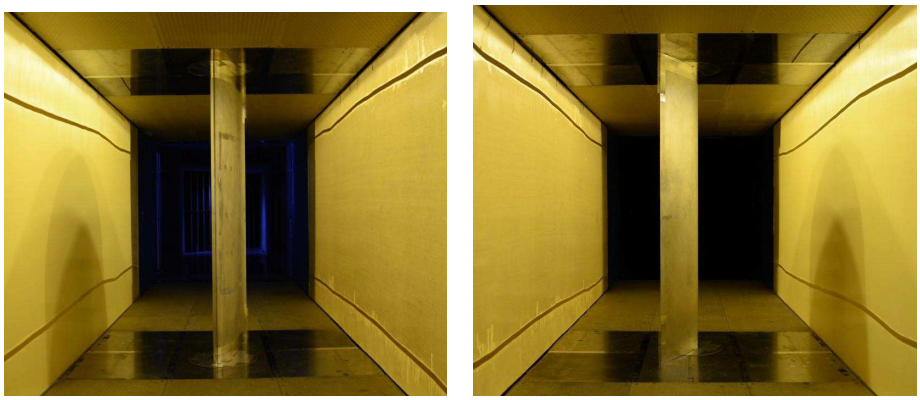

(a) View from upstream (b) View from downstream

Figure 32. The NACA 64-618 airfoil installed in the acoustic test section

7.1.b Acoustic Measurements

A microphone array consisting of 117 microphones was located in the starboard anechoic chamber (see Fig. 33(a)). The microphones were arranged in a 9-armed

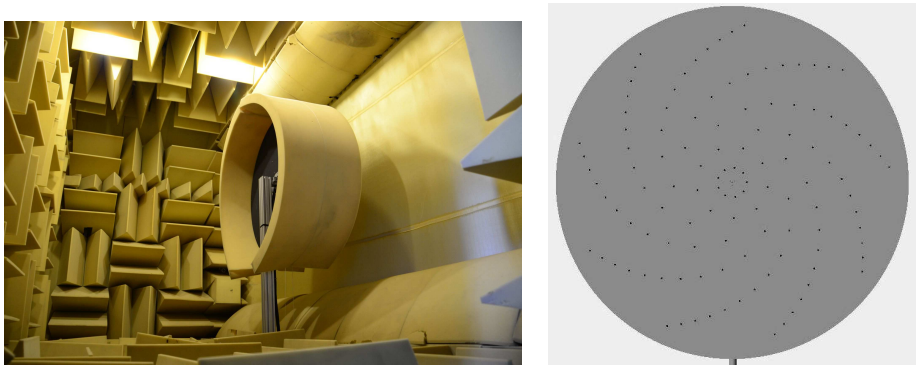

(a) Microphone array in starboard anechoic chamber (b) CAD rendering of the microphone array

Figure 33. Microphone array of AVEC, Inc.

spiral of 13 microphones (see Fig. 33(b)). The diameter of the array disc is 1.1 m. The microphones used in this array are Panasonic model WM-64PNT Electret microphones. These microphones have a flat frequency response from 20-16000 Hz and a sensitivity of $-44 \pm 3dB$ Re 1V/Pa at 1 kHz. All microphones used in the array were calibrated before being installed in the array and selected to be within $\pm 5°$ phase and $\pm 0.4dB$ amplitude from 500 to 16000 Hz.

The microphone array measurements were performed by AVEC, Inc. and the postprocessed data was provided by this company. The postprocessing method according to the description provided by AVEC, Inc. is outlined in the following.

The raw data obtained from the microphone measurement was processed with frequency domain beamforming to extract the sound pressure level of the TE source from the background noise. The time series was measured with a sampling frequency of 51200 Hz during a period of 32 seconds. It was divided into 200 blocks of 8192 samples to compute the averaged cross-spectral density matrix. A classical beamforming algorithm is used to produce maps of the noise distribution in the wind tunnel. To improve the beamforming maps the microphone array was carefully calibrated after installation.

The beamforming maps are integrated to obtain the far field sound pressure spectrum. The integration area was chosen to allow a separation of the TE source from spurious noise caused by the airfoil/wind tunnel junction. It extends 0.6 m of the airfoil span and is centered in the center of the test section. The integral is normalized in a way that the spectrum represents the sound pressure level which a monopole point source at the center of the integration volume causes at the center of the microphone array.

7.2 Validation of a Far-Field Noise Evaluation Using Surface Microphones

This section aims on validating the acoustic formulation of Howe [31] and Amiet with Roger's extensions [57] by comparison of the far field sound pressure spectrum predicted with measured surface pressure statistics as input with the far field sound pressure spectrum measured with the microphone array in the VT experiment.

7.2.a Assessment of the Prediction Method

The far field sound prediction models of Howe and Amiet/Roger, Eq. (20), need the surface pressure PSD close to the trailing edge, the spanwise correlation length and the convection velocity on pressure and suction side of the airfoil as input. For the suction side, the first two quantities can be taken directly taken from the measurements at chord position $x/c = 0.975$. The convection velocity could only be measured with high uncertainty in the low frequency range. Additionally, it varied significantly when measured at different chordwise locations, because the turbulent field is highly inhomogeneous in flow direction and it varied also when measured with different separation of the sensors [12]. In the frequency range up to 800 Hz we used the convection velocity measured between chordwise position $x/c = 0.95$ and $x/c = 0.975$. This implies assuming the convection field remains unchanged between $x/c = 0.95$ and $x/c = 1$ (TE). In the high frequency range we used the empiric expression by Brooks and Hodgson [12]:

$$\frac{U_c}{U_\infty} = 0.39(1 + 2\Delta s/\delta^*)^{0.19} \tag{23}$$

valid in the high-frequency range for a NACA0012 airfoil at AoA $\alpha = 0^o$. In the frequency range between 800 and 2000 Hz we interpolated linearly between the measured value and the value given by Eq. (23).

On the pressure side, only the measured surface pressure PSD at $x/c = 0.95$ is available as input for the acoustic model. The focus of the comparison is therefore on cases where the surface pressure PSD on the pressure side was at least 5 dB lower than the one on the suction side in the frequency range of interest. It comprises basically all cases for effective AoAs of $\alpha_E = 2.6^o$ and higher. Those are also the relevant cases for wind turbine operation. The contribution of the pressure side to the far field sound pressure is then roughly estimated by assuming that the spanwise correlation length is the same as measured on the suction side and the ratio of the convection velocity to flow speed is 0.7 for frequencies up to 1000 Hz, decreasing linearly to 0.4 between frequencies of 1000 and 2000 Hz and then staying constant at 0.4.

Another important issue is where to take the wall pressure statistics as input for each model. In Amiet's model the measurement should represent the surface pressure on the airfoil at the TE without the effect of edge scattering. It was found during the study that the surface pressure PSD measured at $x/c = 0.975$ was free of scattering effects. It is our best estimate of the surface pressure PSD directly at the TE and is used directly as input to the model.

7.2.b Comparison of the Acoustic Models with Microphone Array Response

To compare Howe's and Amiet's model with each other and the measurements we first only evaluated the sound radiated from the suction side. To be able to roughly compare with far field sound measurements we chose a test case in which the surface pressure PSD was about 7dB higher than the one on the pressure side, the NACA 64-618 airfoil at Reynolds number $Re = 1.5$M and effective AoA $\alpha_E = 6.55^o$ (see Fig. 34). The observer is assumed to be situated in the center of the microphone array in the computation with both acoustic models. The full solution of Amiet's model with Roger's extensions (green triangle) produces almost the same solution as the simplified version (red cross). There are only small differences in the low frequency range up to 700 Hz. This is a quite unexpected result, because the simplification was based on the assumption of a large aspect ratio. But in the computation a span of 0.6m was used (to get a result equivalent to the array measurement). It yields an aspect ratio of 1, far from being large. An explanation might be that the observer position is very close to mid span and the $sinc^2$ function

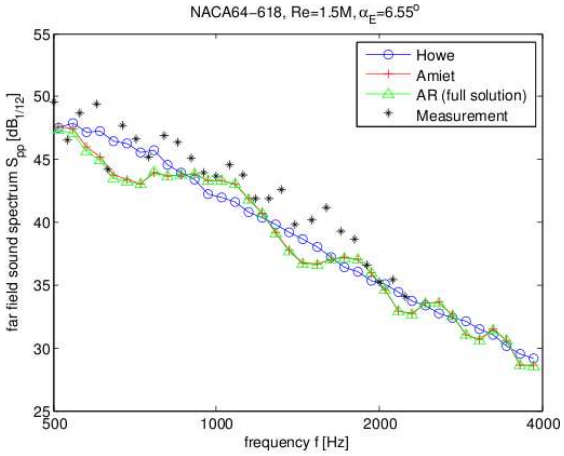

Figure 34. Comparison of the far field sound pressure spectrum for the NACA 64-618 airfoil at $Re = 1.5M$ and $\alpha_E = 6.55^o$ (Observer position for model: center of mic. array; Model: suction side contribution to far field sound only)

of the full solution model is centered about low values of the spanwise wave number and it is narrow enough that the radiation integral is constant in the range of significant spanwise wave numbers.

The main difference between Howe's and Amiet's model is the more elaborated directivity of Amiet's model which is a function of the frequency. In Howe's model the directivity for an infinite high frequency is assumed for all frequencies. The far field sound pressure spectrum predicted with Amiet's model oscillates about the one predicted with Howe's model as 'mean value'. However, those oscillations are not observed in the microphone array measurement. On the other hand, the microphone array is placed quite close to the airfoil compared to its geometric extend. There is a aperture angle of about 36^o from the TE of the airfoil model. The far field sound pressure spectrum measured by the microphone array is an average over its area. This setup can be approximately simulated using a line of 10 observer positions and averaging. The line of observer is placed in the center of the microphone array in the spanwise direction and equally spaced along its chordwise extension. The result is shown in Fig. 35. The Amiet's model yields an nearly identical far field sound pressure spectrum as Howe's model when averaging over 10 observer positions. The difference is less than 0.4 dB, expect in the frequency range lower than 800 Hz. There it can be up to 0.9 dB. The difference compared to the far field sound pressure spectrum measured with the microphone array is up to 2 dB. The difference between the models can be neglected compared to this. The setup with the microphone array positioned close to the airfoil is not suitable to detect directivity effects.

7.2.c Influence of Convection Velocity on Far Field Sound Prediction

The main source of uncertainty in the far field sound pressure prediction using input from the measurement is the unknown convection velocity in the high frequency range. Simulations with different convection velocities assumed constant over the frequency for simplicity were performed for the test case (see Fig. 36). Only the suction side contribution to the far field sound pressure is taken into account. A doubling of the convection velocity corresponds approximately also to a doubling of the far field sound pressure (it can be directly inferred from Eq. (20)), confirmed by the 3 dB difference of the prediction with $U_c/U_\infty = 0.4$

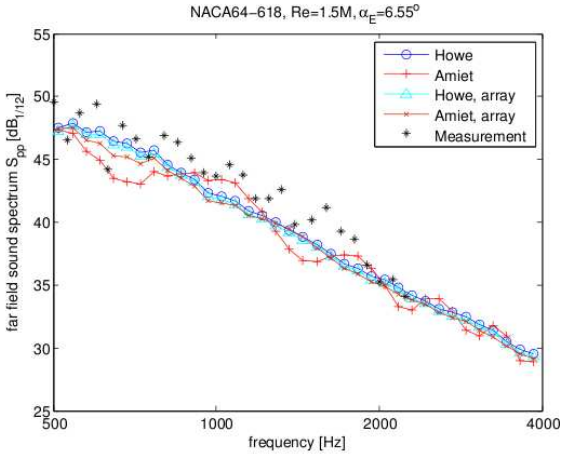

Figure 35. Comparison of the far field sound pressure spectrum for the NACA 64-618 airfoil at $Re = 1.5M$ and $\alpha_E = 6.55^o$ (Observer position for model: center of mic. array; Observer position for model simulating array: spanwise center of mic. array, 10 positions equally spaced over chordwise extend; Model: suction side contribution to far field sound only)

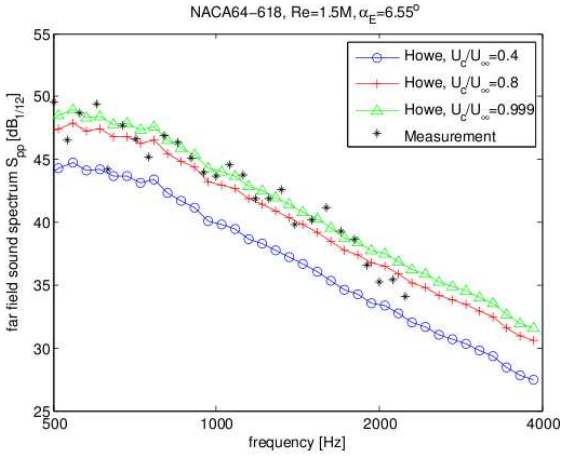

Figure 36. Comparison of the far field sound pressure spectrum for the NACA 64-618 airfoil at $Re = 1.5M$ and $\alpha_E = 6.55^o$ (Observer position: spanwise center of mic. array, 10 positions equally spaced over chordwise extend; Model: suction side contribution to far field sound only)

and $U_c/U_\infty = 0.8$ in Fig. 36.

In the high frequency range at about 2500 Hz the measured sound pressure drops suddenly very strong. This would correspond to sudden drop of the convection velocity in the prediction model. With the present measurements it can not be proven.

7.2.d Comparison of Measurement and Prediction for Several Relevant Cases

The model used in the comparison of the predicted and measured far field sound pressure takes the contribution from both sides into account and is assessed as described in Section 7.2.a. The test cases are chosen that the AoA is in the linear range of the polar and the suction side PSD is at least 5 dB higher than the pressure side PSD. The comparison is displayed in Fig. 37. In all cases, the slope of

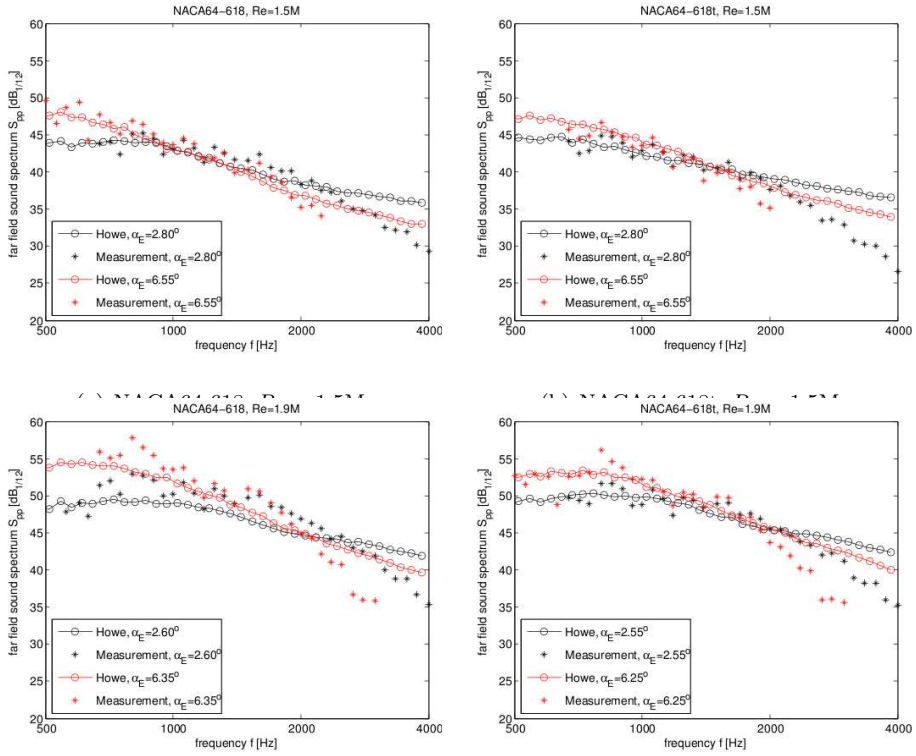

(c) NACA64-618, $Re = 1.9$M (d) NACA64-618t, $Re = 1.9$M

Figure 37. Comparison of measured and predicted far field sound pressure spectrum (Observer position: spanwise center of mic. array, 10 positions equally spaced over chordwise extend; Model: suction and pressure side contribution to far field sound)

the predicted far field sound pressure spectrum is flatter than the measured one. It is higher in the high frequency range and lower in the low frequency range. The difference for high frequencies can be due to a bad estimate of the convection velocity. Improving the setup to measure the convection velocity at higher frequencies can improve the prediction. In the low frequency range, say up to 2000 Hz, the predictions are excellent.

Another point of controversy in the model is the fulfillment of the Kutta condition at the TE in the high frequency range. If the Kutta condition is fulfilled suction and pressure side can be treated separately. If the Kutta condition is not fulfilled the flow around the TE has to be treated as a whole and a model dealing with different pressure distributions on both sides is necessary. The results above showed that the prediction of the far field sound pressure in the high frequency range is better if only the suction side contribution is taken into account. This leads to the speculation that the flow at the TE is more complex in reality and a simple summation of the contribution of both sides to the far field sound is not appropriate.

Another reason for the difference could be the inhomogeneity of the surface pressure PSD close to the TE. The model assumption is clearly violated.

7.3 Validation of a Noise Optimized Airfoil Design

As described in the previous section, the wind tunnel measurements were performed at the Virginia Tech Stability Wind Tunnel. During this campaign the airfoil design exposed in Section 6 could be tested. Both the aerodynamic and

acoustic characteristics of the original and optimized airfoils are compared in the following.

7.3.a Aerodynamic Analysis of Original and Optimized Airfoils

The lift curves as a function of the relative angle of attack α_0 obtained at each tested inflow velocity, including the case of the tripped airfoil for the intermediate one, are displayed in Figs. 38(a-d). There exists a quite good agreement between the experimental data and the CFD calculations, as least in the linear region. However, the slow lift curve slope decrease as the maximum lift is approached for the original tripped airfoil measured in the wind tunnel is not captured by the CFD solver. As the curves approach maximum lift, it can be observed in the measurements that the optimized airfoil reaches higher values of this maximum lift, whereas the lift curve of the original airfoil stagnates around this maximum lift. At higher angles of attack, the optimized airfoil present a stall behavior with a distinct drop in lift. Such behavior was basically already predicted by the CFD and Xfoil calculations in Section 6.3.

It is thereby confirmed that the optimized airfoil provides slightly better aerodynamic performances as long as one considers maximum lift as an important design characteristics and if somewhat more abrupt stall characteristics are acceptable. Since drag could not be measured in the wind tunnel facility, the conclusions drawn in the previous section in this respect can not be directly validated. However, the good agreement between measured and CFD calculated lift results in this Section contributes to surmise that this also holds in reality.

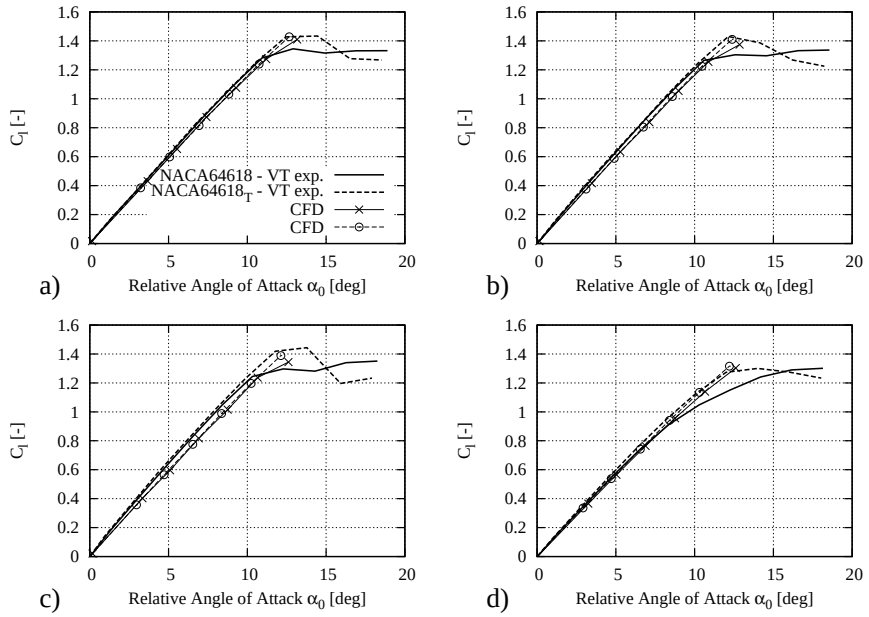

Figure 38. Lift as function of α_o: a) $U_\infty = 30\ m/s$, b) $U_\infty = 45\ m/s$, c) $U_\infty = 60\ m/s$, d) $U_\infty = 45\ m/s$ with tripped airfoil.

It is important to note here that the CFD calculations performed in the free transition case were not able to reproduce the transition locations observed in the wind tunnel. The latter could be detected using high-frequency microphones flush-mounted in the measuered airfoil section making use of the technique developed by Døssing [20]. Therefore all the CFD calculation results that are presented in this paper and referred to as clean airfoil were obtained by enforcing transition at

the same location than the one observed in the wind tunnel experiment.

7.3.b Acoustic Analysis of Original and Optimized Airfoils

As described in the beginning of this section, the noise emitted at the trailing edge of the airfoils has been measured simultaneously with the aerodynamic characteristics.

The noise spectra measured in the various velocity and airfoil configurations are compared to those calculated with the CFD/TNO model. The angles of attack are equal to those obtained in the wind tunnel (including wind tunnel corrections). In Figs. 39(a-d) the spectra are plotted for relative angles of attack approximately equal to $\alpha_0 \approx 10^o$. As explained earlier, exact relative angles of attack can not be achieved during the wind tunnel measurements since these were performed at discrete geometric angles of attack with 2^o intervals, the wind tunnel corrections obviously not being known in advance as dependent it depends on the loading on the airfoil. Therefore, the above figures do not provide a fair comparison between the original and optimized airfoils. Nevertheless, the differences between the original and the optimized airfoil are quite small. It is however clear that the CFD/TNO model over-estimates the measured noise spectra, in particular at higher angles of attack.

In order to provide a more objective comparison of the results, the noise spectra are integrated along a specified spectral band for all measured and calculated angles of attack. The results are then plotted as a function of the measured or calculated lift for the corresponding case. Fig. 40 display the integrated spectra over the whole frequency range where measurements are reliable, that is $600 < f < 3000\,\mathrm{Hz}$. The spectra obtained from the CFD/TNO model are accordingly integrated over the same frequency interval. It can be observed that the CFD/TNO calculations consistently overpredict the measured integrated spectra. In addition, comparisons between the original and optimized airfoil show opposite tendencies whether the model results or the measurements are considered, except for the tripped case (Fig. 40(d)). As for the measurements, as long as the flow remains attached, the optimized airfoil performs always better than the original airfoil when the airfoil is not tripped. Indeed, at equal lift coefficient C_l the former airfoil exhibits lower integrated noise values. This noise reduction remains rather modest and ranges from 0.5 dB for the low angles of attack and low velocity to 2 dB for the highest wind speed. However, for the highest angle of attack where stall initiates, the tendency is inversed and the original airfoil becomes less noisy than the optimized one in the case without tripping, and vice-versa for the tripped case. Nevertheless, it is clear in the figures that the optimized airfoil can reach quite larger maximum lift without significant change in noise emission.

The CFD/TNO calculations yield different results. It appears that the optimized airfoil is always more noisy, which is in accordance with the measurements in the tripped case, but not in the free transition case.

7.3.c Conclusions

An optimization procedure was conducted in order improve the TE noise characteristics of a standard wind turbine airfoil without compromising its aerodynamic performances. The optimization code uses the airfoil flow solver Xfoil to calculate the turbulent BL characteristics that are subsequently used to evaluate the TE noise. The optimization algorithm succeeded in reducing the cost function based on this model. However, CFD calculations conducted a posteriori did not confirm that the expected noise reduction could be achieved.

The two airfoil prototypes were tested in an acoustic wind tunnel facility. The new airfoil design exhibits quite weak TE noise reductions compared to the original

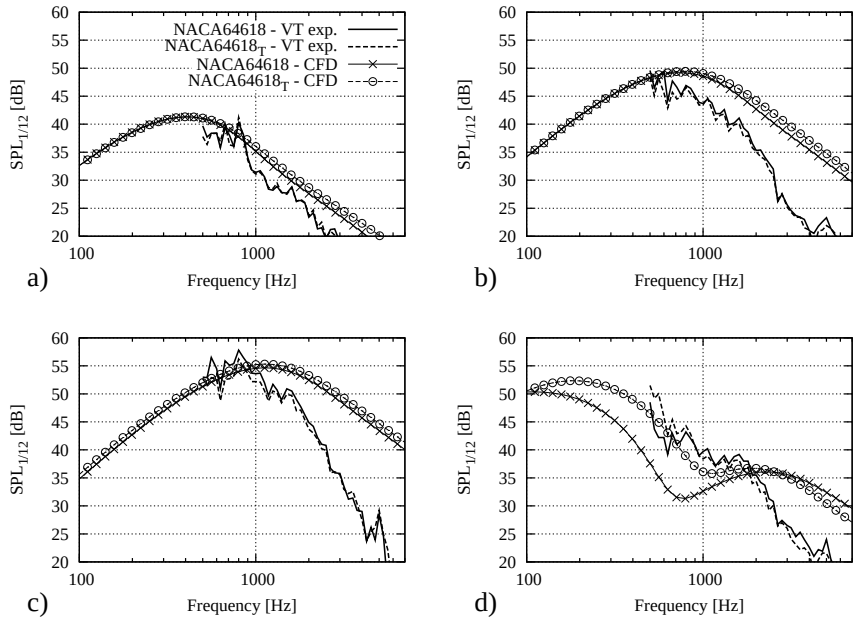

Figure 39. Noise spectra (in $1/12^{th}$ octave bands) at $\alpha_o \approx 10^o$: a) $U_\infty = 30\,m/s$, b) $U_\infty = 45\,m/s$, c) $U_\infty = 60\,m/s$, d) $U_\infty = 45\,m/s$ with tripped airfoil.

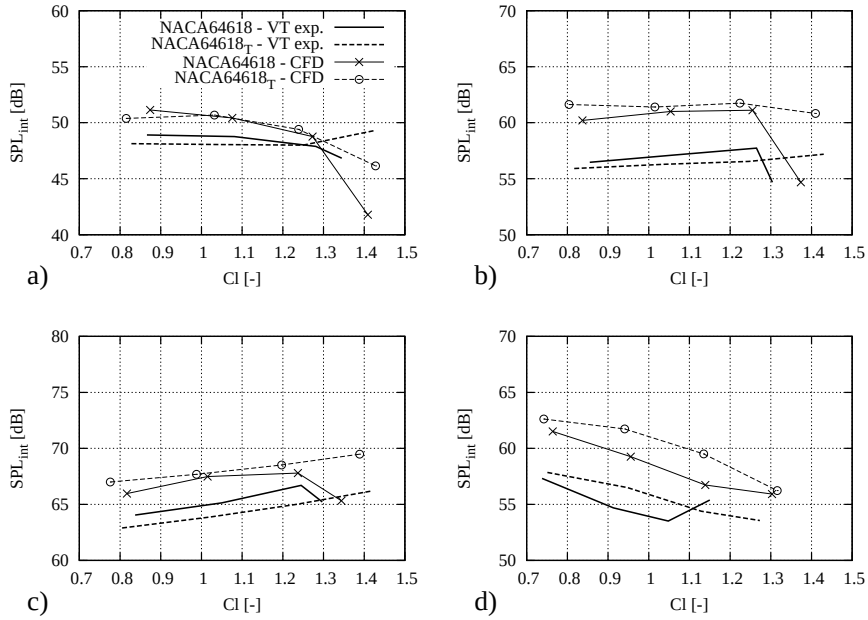

Figure 40. Integrated noise spectra (600 to 3000 Hz) as function of lift: a) $U_\infty = 30\,m/s$, b) $U_\infty = 45\,m/s$, c) $U_\infty = 60\,m/s$, d) $U_\infty = 45\,m/s$ with tripped airfoil.

airfoil, and actually noise increase in the tripped case. Not however that tripping an airfoil can have severe effects on the turbulent BL that are difficult to model and predict.

Therefore, in the future, an optimization method using the CFD flow calculations should be considered in the design process in order to achieve the expected substantial noise reductions.

Nevertheless, the new airfoil design exhibits better aerodynamic performances than the original one. Slightly better lift in the linear region and relatively im-

portant maximum lift increase were observed, in particular when using the more accurate CFD code as a flow solver, as a function of relative angle of attack. In addition, large lift-to-drag ratio increase around design relative angle of attack were also observed.

Some of the difficulties faced during this study are related to the particular behavior of the NACA64618 airfoil. Indeed, this airfoil is part of the group of so-called 'laminar' airfoil. These are characterized by a late transition, i.e. usually far downstream of the trailing edge. This phenomenon is, as we found out, not easily reproduced by the standard transition models, or at least the calculation results can become very sensitive to other parameters due to the uncertainty associated to the transition location.

As a conclusion about the design process, it can be argued that benificial aerodynamic features have been obtained without compromising the acoutic characteristics, and in most cases even slightly reducing the TE noise emission. However, better noise reduction could probably be obtained if using a CFD code as a flow solver during the design process instead of the Xfoil code which results seem not accurate enough for TE noise calculations in this case.

Acknowledgments

The authors would like to thank LM Wind Power A/S for their participation in the above project, and in particular Jesper Madsen and Poul Kramer for their support in designing the new airfoil and manufacturing the airfoil section models.

The authors would also like to thank Prof. William Devenport for allowing us to use the VT Stability Wind Tunnel at the Aerospace and Ocean Engineering Department of Virginia Tech University. The operation of the wind tunnel was supervised by Bill Oetjens. Acoustic measurements were conducted by Dr. Patricio Ravetta from AVEC, Inc. (Blacksburg, VA).

Measurements in the above wind tunnel would not have been possible without the technical competences of Per Hansen and its help in setting up the experimental rig and fixing the numerous problems that arose.

8 Conclusions

As part of this project, an initial experiment was conducted during which detailed boundary layer measurements were performed with a hot-wire set-up together with surface pressure microphones. Important imformations concerning the turbulence structure of the boundary layer were collected. The classical trailing edge noise model, the so-called TNO-model which is also able to predict surface pressure fluctuations, proved to perform poorly against the measured pressure spectra. Finally, measuring noise using hot-wires located outside the turbulent boundary layer proved impractical due to the presence of high background noise levels.

The above measurement data constitute the basis to theoretical development and improvement of the original TNO-model. Turbulence anisotropy and boundary layer mean pressure gradient were introduced in the model formulation. The model was tuned to fit the above measurement data. The new formulation significantly improved the model prediction capabilities.

A measurement technique based on microphone flush-mounted beneath the surface of the airfoil near the trailing edge was developed. This technique is designed to estimate the far-field noise radiated by the trailing edge without having to actually perform measurements in the far-field. The methodology relies on a tubing set-up so that microphones can be located very close to the trailing edge. This tubing system necessitates an accurate calibration of the microphones. Such a calibration methodology was also developed.

A design method based on an existing optimization program was developed to include noise optimization of airfoil sections. A new airfoil design was proposed. The method made use of the original TNO-model. In addition, the airfoil flow solver Xfoil which is appropriate for the aerodynamic design of airfoils was used.

A second and last experiment was conducted in the acoustic wind tunnel of the Virginia Tech University. In this tunnel, a set-up for the measurement of far-field noise with a microphone array is available. The surface pressure measurement technique close to the trailing edge using the above new tubing system was tested and the calibration technique was validated. The measurement methodology proposed above to evaluate far-field noise from these surface microphones was also validated and gave good results. In addition, the new airfoil design proposed above was tested and compared to a reference airfoil. The aerodynamic characteristics of the new airfoil were improved, but noise reduction were not as important as expected. This last setback is partly attributed to the flow solver Xfoil together with the original TNO model being unable to accurately predict the BL turbulence characteristics.

9 Perspectives

Acoustic emissions from wind turbines have nowadays become a major concern for wind turbine manufacturers and operators. Indeed, the growing demand for renewable energy sources, combined with the significant increase of wind turbine sizes over the last two decades to meet this demand, have raised important problems associated to the strict noise regulations that also have to be considered when installing wind turbines.

The present study has brought two important contributions that can readily be applied in the industry and help mitigate the above-mentioned problems:

1. A measurement methodology for evaluating trailing-edge noise emission using

microphones flush-mounted in the airfoil/blade itself has been developped and tested in an acoustic wind tunnel.

2. A methodology for low-noise airfoil design has been developped. As a test case, a noise optimized airfoil has been designed and tested in the above acoustic wind tunnel.

As far as the first contribution is concerned, this should have two important impacts on the commercial activities within wind turbine developers and manufacturers. Firstly, this technique can be used in a classical wind tunnel that is not designed for acoustic measurements. It should be mentioned here that all danish wind turbine and wind turbine blade manufacturers do not own such an acoustic facility themselves. In order to perform acoustic measurements, they have to rent an appropriate facility abroad. As a results, the above measurement technique can make the acoustic design and validation of new airfoil sections cheaper and faster. Secondly, this technique can also be used on actual wind turbines to assess their noise emission. This concept was actually tested within the DANAERO project [39] for which a wind turbine was equipped with similar microphones that were flush-mounted on the turbine blades as in the present experimental set-up. The present project can be considered on one side as a validation of the acoustic mechanism involved with trailing-edge noise emission in controlled experimental conditions, which cannot be performed on a real-life wind turbine since the various wind turbine noise sources are very difficult to distinguish from each other and/or from the ambient noise. On the other side, it can be considered as a feasibility study for the evaluation of noise using these microphones on an actual wind turbine.

As for the second contribution of this project, the results of the present study proved that the airfoil flow solver Xfoil is a too crude approximation for the boundary layer calculations. Indeed, it appears that a more advanced model such as CFD is necessary to correctly capture the physics underlying the noise mechanism. Nevertheless, since the simplified model Xfoil is still valid to predict the airfoil aerodynamic characteristics, the newly designed airfoil proved to exhibit better aerodynamic features in term of maximum lift. However, the expected noise reduction were not as substantial as expected for the reason mentioned above. Still, detectable noise reductions were observed for the new airfoil without tripping devices. The pitfalls met during this study should be taken into account for new design concepts. This should contribute in the future to better noise optimized airfoils.

On the commercial side and as a follow-up to this project, LM Wind Power is conducting further investigations for the design of low-noise airfoil profiles. It is intended that such profiles will be used on commercial wind turbines within a timeframe of approximately 2 years. On the technological side, LM Wind Power is still developing the methodology to experimentally verify airfoil noise in wind tunnels. These activities are part of a different EUDP-funded project named: 'Design of New Generation Wind Turbine Rotors (NextRotor)'.

References

[1] R. K. Amiet, *Noise due to Turbulent Flow Past a Trailing Edge*, J. Sound Vib. **47** (1976), no. 3, 387–393.

[2] C. D. Aubertine and J. K. Eaton, *Turbulence Development in a Non-Equilibrium Turbulent Boundary Layer With Mild Adverse Pressure Gradient*, J. Fluid Mech. **532** (2005), 345–364.

[3] B. S. Baldwin and T. J. Barth, *A One Equation Turbulence Transport Model for High Reynolds Number Wall-Bounded Flows*, TM 102847, AIAA, 1990.

[4] J. Bardina, J. H. Ferziger, and W. Reynolds, *Improved Subgrid Scale Models for Large-Eddy Simulations*, AIAA Paper 80-1357, 1980.

[5] F. Bertagnolio, *NACA0015 Measurements in LM Wind Tunnel and Turbulence Generated Noise*, Tech. Rep. Risø-R-1657(EN), Risø-DTU, Roskilde, Denmark, November 2008.

[6] ———, *Boundary Layer Measurements of the NACA0015 and Implications for Noise Modeling*, Tech. Rep. Risø-R-1761(EN), Risø-DTU, Roskilde, Denmark, January 2011.

[7] ———, *Experimental Investigation and Calibration of Surface Pressure Modeling for Trailing Edge Noise*, Proc. of Inter-Noise 2011 Conf. (Osaka, Japan), September 2011.

[8] F. Bertagnolio and A. Fischer, *Noise Optimization of a Wind Turbine Airfoil and Wind Tunnel Aerodynamic and Acoustic Validation*, (To be submitted to Wind Energy).

[9] F. Bertagnolio, A. Fischer, and W. J. Zhu, *Tuning of Turbulent Boundary Layer Anisotropy for Improved Surface Pressure and Trailing-Edge Noise Modeling*, AIAA J. (Submitted).

[10] W. K. Blake, *Mechanics of Flow-Induced Sound and Vibration, Vol.I and II*, vol. in Applied Mathematics and Mechanics, Frenkiel, F.N. and Temple, G. (eds.), Academic Press, 1986.

[11] K. A. Braun, N. J. C. M. v.d. Borg, A. G. M. Dassen, A. Gordner, and R. Parchen, *Noise Reduction by Using Serrated Trailing Edges*, Proc. of the EWEC'97 Conference (Dublin, Ireland), 1997.

[12] T. F. Brooks and T. H. Hodgson, *Trailing Edge Noise Prediction from Measured Surface Pressures*, J. Sound Vib. **78** (1981), no. 1, 69–117.

[13] K.L. Chandiramani, *Diffraction of Evanescent Waves with Applications to Aerodynamically Scattered Sound and Radiation from Unbaffled Plates*, J. Acoust. Soc. Am. **55** (1974), no. 1, 19–29.

[14] D.M. Chase, *Sound Radiated by Turbulent Flow off a Rigid Half-Plane as Obtained from a Wavevector Spectrum of Hydrodynamic Pressure*, J. Acoust. Soc. Am. **52** (1972), no. 3B, 1011–1023.

[15] P. Chaviaropoulos, B. Bouras, G. Leoutsakos, and K. D. Papailiou, *Design of Optimized Profiles for Stall Regulated HAWTs Part 1: Design Concepts and Method Formulation*, Wind Engineering **17** (1993), no. 6, 275–287.

[16] G. M. Corcos, *Resolution of Pressure in Turbulence*, J. Acoust. Soc. Am. **35** (1963), no. 2, 192–199.

[17] G. B. Dantzig, *Linear Programming and Extensions*, Princeton University Press, Princeton, N.J., 1963.

[18] A. G. M. Dassen, R. Parchen, J. Bruggeman, and F. Hagg, *Results of a Wind Tunnel Study on the Reduction of Airfoil Self-noise by the Application of Serrated Blade Trailing Edges*, Proc. of the European Union Wind Energy Conference and Exhibition (Göteborg, Sweden), 1996.

[19] J. W. Deardorff, *A Numerical Study of Three-Dimensional Turbulent Channel Flow at Large Reynolds Numbers*, J. Fluid Mech. **41** (1970), 453–480.

[20] M. Døssing, *High Frequency Microphone Measurements for Transition Detection on Airfoils*, Tech. Rep. Risø-R-1645(EN), Risø-DTU, Roskilde, Denmark, June 2008.

[21] M. Drela, *Low Reynolds Number Aerodynamics*, vol. 54, ch. XFOIL: An Analysis and Design System for Low Reynolds Number Airfoils, pp. 1–12, Mueller, T.J. (ed.), Lecture Notes in Engineering, Springer-Verlag, Berlin, 1989.

[22] M. Drela and M. B. Giles, *Viscous-Inviscid Analysis of Transonic and Low Reynolds Number Airfoils*, AIAA Journal **25** (1987), no. 10, 1347–1355.

[23] A. Fischer, *Experimental Characterization of Airfoil Boundary Layers for Improvement of Aeroacoustic and Aerodynamic Modeling*, PhD Thesis, Risø-R-****-(EN), Risø-DTU, Roskilde, Denmark, Nov. 2011.

[24] A. Fischer, F. Bertagnolio, C. Bak, and H. Aa. Madsen, *Surface Pressure Measurements on a NACA0015 Airfoil Compared to Computations with the TNO Trailing Edge Noise Model*, Proc. of the Torque 2010 'The Science of Making Torque from Wind' Conf. (EWEA) (Crete, GR), June 2010, pp. 81–92.

[25] P. Fuglsang and C. Bak, *Development of the Risø Wind Turbine Airfoils*, Wind Energy **7** (2004), 145–162.

[26] P. Fuglsang and K. S. Dahl, *Multipoint Optimization of Thick High Lift Airfoil Wind Turbines*, Proc. EWEC'97 (Dublin, Ireland), 1997.

[27] R. Guastavino, *On-site Microphone Calibration for 'Low Noise Airfoil' EUDP Project J.nr.64009-0272*, Tech. Rep. (Private Communication), Brüel & Kjær Sound & Vibration Measurement A/S, Nærum, Denmark, 2010.

[28] G. Guidati, *Design and Testing of Acoustically Optimized Airfoils for Wind Turbines*, Proc. of the 1999 EWEC Conference (Nice, France), March 1999.

[29] G. Guidati and S. Wagner, *Design of Reduced Noise Airfoils for Wind Turbines*, Proc. of the ECCOMAS 2000 Conference (Barcelona, Spain), 2000.

[30] D. M. Hill and A. D. Garrad, *Design of Aerofoils for Wind Turbine Use*, In IEA Symposition on Aerodynamics of Wind Turbines (Lyngby, Denmark), 1988.

[31] M. S. Howe, *A Review of the Theory of Trailing Edge Noise*, J. Sound Vib. **61** (1978), no. 3, 437–465.

[32] ———, *Noise Produced by a Sawtooth Trailing Edge*, J. Acoust. Soc. Am. **90** (1991), no. 1, 482–487.

[33] R. I. Issa, *Solution of the Implicitly Discretized Fluid Flow Equations by Operator-Splitting*, J. Computational Physics **62** (1985), no. 1, 40–65.

[34] F. E. Jørgensen, *How to Measure Turbulence with Hot-Wire Anemometer - A Practical Guide*, Available at: http://www.dantecdynamics.com/Admin/Public, 2002.

[35] B. E. Launder and B. I. Sharma, *Application of the Energy Dissipation Model of Turbulence to the Calculation of Flow Near a Spinning Disc*, Letters in Hear and Mass Transfer **1** (1974), no. 2, 131–138.

[36] D. K. Lilly, *The Representation of Small-Scale Turbulence in Numerical Simulation Experiments*, Proceedings of the IBM scientific Computing Symposium on Environmental Sciences, 1974, pp. 195–210.

[37] T. Lutz, A. Herrig, W. Würz, M. Kamruzzaman, and E. Krämer, *Design and Wind-Tunnel Verification of Low-Noise Airfoils for Wind Turbines*, AIAA Journal **45** (2007), no. 4, 779–785.

[38] D. A. Lynch, W. K. Blake, and T. J. Mueller, *Turbulence Correlation Length-Scale Relationships for the Prediction of Aeroacoustics Response*, AIAA Journal **43** (2005), no. 6, 1187–1197.

[39] H. Aa. Madsen, C. Bak, U. S. Paulsen, M. Gaunaa, P. Fuglsang, J. Romblad, N. A. Olesen, P. Enevoldsen, J. Laursen, and L. Jensen, *The DAN-AERO MW Experiments - Final report*, Tech. Rep. Risø-R-1726(EN), Risø-DTU, Roskilde, Denmark, September 2010.

[40] Y. Mary and P. Sagaut, *Large-Eddy Simulation of Flow Around an Airfoil Near Stall*, AIAA J. **40** (2002), no. 6, 1139–1145.

[41] J. Mathieu and J. Scott, *Introduction to Turbulent Flow*, Cambridge University Press, Cambridge (UK), 2000.

[42] L. Meirovich, *Elements of Vibration Analysis*, McGraw Hill, 1975.

[43] F. R. Menter, *Zonal Two-Equations k–ω Turbulence Models for Aerodynamic Flows*, Proceedings, AIAA Paper 93-2906, 1993.

[44] J. A. Michelsen, *Basis3D - A Platform for Development of Multiblock PDE Solvers*, Tech. Rep. AFM 92-05, Technical University of Denmark, 1992.

[45] J. A. Michelsen, *Basis3D - A Platform for Development of Multiblock PDE Solvers*, Tech. Rep. AFM 92-05, Technical University of Denmark, Lyngby, Denmark, 1992.

[46] J. A. Michelsen, *Block Structured Multigrid Solution of 2D and 3D Elliptic PDE's*, Tech. Rep. AFM 94-06, Technical University of Denmark, 1994.

[47] J. A. Michelsen, *Block Structured Multigrid Solution of 2D and 3D Elliptic PDE's*, Tech. Rep. AFM 94-06, Technical University of Denmark, Lyngby, Denmark, 1994.

[48] P. Moriarty, G. Guidati, and P. Migliore, *Prediction of Turbulent Inflow and Trailing-Edge Noise for Wind Turbines*, Proc. of the 11^{th} AIAA/CEAS Aeroacoustics Conf. (Monterey, CA), AIAA Paper 2005-2881, 2005.

[49] R. L. Panton and J. H. Linebarger, *Wall Pressure Spectra Calculations for Equilibrium Boundary Layers*, J. Fluid Mech. **65** (1974), no. 2, 261–287.

[50] H. D. Papenfuß, *Aerodynamic Commissioning of the New Wind Tunnel at LM Glasfiber A/S (Lunderskov); Private Communication*, Property of LM Glasfiber, June 2006.

[51] R. Parchen, *Progress report DRAW: A Prediction Scheme for Trailing-Edge Noise Based on Detailed Boundary-Layer Characteristics*, TNO Rept. HAG-RPT-980023, TNO Institute of Applied Physics, The Netherlands, 1998.

[52] S. Perénnès, *Caractérisation des sources de bruit aérodynamique à basses fréquences de dispositifs hypersustentateurs*, Ph.D. thesis, Ecole Centrale de Lyon, 1999.

[53] L. Ta Phuoc, *Modèles de Sous-Maille Appliqués aux Ecoulements Instationnaires Décollés*, Proc. of the DRET Conference: Aérodynamique Instationnaire Turbulente-Aspects Numériques et Expérimentaux (LIMSI/CNRS, Orsay, France), 1994, Tech. Rep. 93074, pp. 1–38.

[54] U. Piomelli and E. Balaras, *Wall-layer Models for Large-Eddy Simulations*, Annual Review of Fluid Mechanics **34** (2002), 349–374.

[55] C. Polacsek, G. Reboul, V. Clair, T. Le Garrec, and H. Deniau, *Turbulence-Airfoil Interaction Noise Reduction Using Wavy Leading Edge: An Experimental and Numerical Study*, Proc. of Inter-Noise 2011 Conf. (Osaka, Japan), September 2011.

[56] C. M. Rhie and W. L. Chow, *Numerical Study of the Turbulent Flow Past an Airfoil with Trailing Edge Separation*, AIAA Journal **21** (1983), no. 11, 1525–1532.

[57] M. Roger and S. Moreau, *Back-Scattering Correction and Further Extensions of Amiet's Trailing-Edge Noise Model. Part 1: Theory*, J. Sound Vib. **286** (2005), no. 3, 477–506.

[58] P. Sagaut, *Large Eddy Simulation for Incompressible Flows, An Introduction*, Springer-Verlag, 1999.

[59] J. G. Schepers, A. Curvers, S. Oerlemans, K. Braun, T. Lutz, A. Herrig, W. Wuerz, A. Mantesanz, L. Garcillan, M. Fischer, K. Koegler, and T. Maeder, *SIROCCO: Silent Rotors by Acoustic Optimization*, Tech. Rep. ECN-M-07-064, ECN, The Netherlands, 2007.

[60] W. Z. Shen, J. A. Michelsen, Sørensen N. N., and J. N. Sørensen, *An Improved SIMPLEC Method on Collocated Grids for Steady and Unsteady Flow Computations*, Numerical Hear Transfer, Part B **43** (2003), no. 3, 221–239.

[61] W. Z. Shen, J. A. Michelsen, and J. N. Sørensen, *An Improved Rhie-Chow Interpolation for Unsteady Flow Computations*, AIAA Journal **39** (2001), no. 12, 2406–2409.

[62] J. Smagorinsky, *General Circulation Experiments with the Primitive Equations*, Mon. Weather Rev. **91** (1963), 99–164.

[63] N. N. Sørensen, *General Purpose Flow Solver Applied to Flow over Hills*, PhD Thesis, Tech. Rep. Risø-R-827(EN), Risø National Laboratory, Roskilde, Denmark, June 1995.

[64] N. N. Sørensen, *CFD Modelling of Laminar-turbulent Transition for Airfoils and Rotors Using the $\gamma - Re_\theta$ Model*, Wind Energy **12** (2009), no. 8, 715–733.

[65] P. R. Spalart and S. R. Allmaras, *A One-Equation Turbulence Model for Aerodynamic Flows*, AIAA Paper 92-0439, 1992.

[66] P. R. Spalart, W.-H Jou, M. Stretlets, and S. R. Allmaras, *Comments on the Feasibility of LES for Wings and on the Hybrid RANS/LES Approach*, Proceedings of the First AFOSR International Conference on DNS/LES, Advances in DNS/LES, 1997.

[67] J. L. Tangler and D. M. Somers, *Status of the Special-Purpose Airfoil Families*, Tech. Rep. SERI/TP-217-3264; CONF-871062-9, Solar Energy Research Inst., CO (USA); Airfoils, Inc., VA (USA), December 1987.

[68] W. A. Timmers and R. P. J. O. M. Van Rooy, *Thick Airfoils for HAWTs*, Journal of Wind Engineering and Industrial Aerodynamics **39** (1992), no. 1-3, 151–160.

[69] D. C. Wilcox, *Reassessment of the Scale-Determining Equation for Advanced Turbulence Models*, AIAA Journal **26** (1988), no. 11, 1299–1310.

[70] J. E. Ffowcs Williams and L. H. Hall, *Aerodynamic Sound Generation by Turbulent Flow in the Vicinity of a Scattering Half Plane*, J. Fluid Mech. **40** (1970), no. 4, 657–670.

DTU Wind Energy
Technical University of Denmark

Frederiksborgvej 399
4000 Roskilde
Denmark
Phone +45 4677 5024

www.vindenergi.dtu.dk